

Causal Network Models of SARS-CoV-2 Expression and Aging to Identify Candidates for Drug Repurposing

Anastasiya Belyaeva^{1#}, Louis Cammarata^{2#}, Adityanarayanan Radhakrishnan^{1#},
Chandler Squires¹, Karren Dai Yang¹, G.V. Shivashankar^{3,4}, Caroline Uhler^{1,3*}

¹Massachusetts Institute of Technology, U.S.A.

²Harvard University, U.S.A.

³ETH Zurich, Switzerland

⁴Paul Scherrer Institute, Switzerland

#Equal contribution.

*To whom correspondence should be addressed; E-mail: cuhler@mit.edu.

Abstract Given the severity of the SARS-CoV-2 pandemic, a major challenge is to rapidly repurpose existing approved drugs for clinical interventions. While a number of data-driven and experimental approaches have been suggested in the context of drug repurposing, a platform that systematically integrates available transcriptomic, proteomic and structural data is missing. More importantly, given that SARS-CoV-2 pathogenicity is highly age-dependent, it is critical to integrate aging signatures into drug discovery platforms. We here take advantage of large-scale transcriptional drug screens combined with RNA-seq data of the lung epithelium with SARS-CoV-2 infection as well as the aging lung. To identify robust druggable protein targets, we propose a principled causal framework that makes use of multiple data modalities. Our analysis highlights the importance of serine/threonine and tyrosine kinases as potential targets that intersect the SARS-CoV-2 and aging pathways. By integrating transcriptomic, proteomic and structural data that is available for many diseases, our drug discovery platform is broadly applicable. Rigorous in vitro experiments as well as clinical trials are needed to validate the identified candidate drugs.

Candidates for drug repurposing have mainly been identified based on an understanding of their pharmacology or based on retrospective analyses of their clinical effects. Recently, also more systematic computational methods combined with large-scale experimental screens have been employed [1]. The Connectivity Map (CMap) containing gene expression profiles generated by dosing thousands of small molecules, including many FDA approved compounds, in a number of human cell lines has been particularly valuable in this regard [2]. Common computational approaches include signature matching, where the signature of a drug is determined for example using CMap and compared to the reverse signature of a disease to identify drugs with high correlation [3]. In addition, approaches to identify drug or disease networks based on known pathways, protein-protein interactions, gene expression or genome-wide association studies have also been employed [4, 5, 6]. To capitalize on the abundance of data, it is critical to develop computational platforms that can integrate different data modalities including gene expression, drug targets and signatures, as well as protein-protein interactions. In addition, a drug represents an intervention in the system and only a causal framework allows predicting the effect of an intervention. It is therefore critical to capitalize on recent advances in causal inference [7, 8] in particular with respect to the use of interventional data [9, 10, 11, 12].

Given the current coronavirus disease 2019 (COVID-19) crisis, there is an urgent need for the development of robust drug repurposing methods. Coronaviruses belong to the family of positive-strand RNA-viruses. While most coronaviruses infect the upper respiratory tract and cause mild illness, they can have serious effects as exemplified by the severe acute respiratory syndrome coronavirus (SARS-CoV) epidemic and now the SARS-CoV-2 pandemic [13]. Recent studies have shown that coronaviruses use canonical inflammatory pathways (e.g. NF- κ B) of the host cell for their replication, while simultaneously dampening their outward inflammatory signaling [14, 15]. This delicate partial up and down-regulation of inflammatory pathways by coronaviruses has represented major challenges for therapeutic interven-

tions [16]. While the infection rates for these viruses are similar among different age groups, the morbidity and fatality rates are significantly higher in the aging population [17, 18]. The respiratory system of aging individuals is characterized by alterations of tissue stiffness [19]. Notably, recent micropatterning experiments have shown that cells subjected to substrates of different stiffness stimulated with the same cytokine (TNF- α) exhibit different downstream NF- κ B signaling [20]. In a recent commentary, we outlined that the cross-talk between coronavirus infection and cellular aging could play a critical role in the replication of the virus in host cells by differentially intersecting with NF- κ B signaling [21]. This suggests that efforts for drug repurposing should analyze SARS-CoV-2 infected host cell expression programs in conjunction with aging-dependent programs. While a number of studies are underway that investigate viral integration/replication and interactions with the host cell [6, 22], to our knowledge the interplay of SARS-CoV-2 host response and aging has not been explored in the context of drug development and repurposing.

In this paper, we propose a novel computational platform for drug repurposing, which integrates transcriptomic, proteomic and structural data with a principled causal framework, and we apply it in the context of SARS-CoV-2 (Fig. 1). Given the age-dependent pathogenicity of SARS-CoV-2, we first identify genes that are differentially regulated by SARS-CoV-2 infection and aging based on bulk RNA-seq data from [23, 24]. We then use an autoencoder, a type of artificial neural network used to learn data representations in an unsupervised manner [25, 26], to embed the CMap data together with the SARS-CoV-2 expression data for signature matching to obtain an ordered list of FDA approved drugs. In particular, we show that overparameterized autoencoders align drug signatures from different cell types and thus allow constructing synthetic interventions [27, 28] by translating the effect of a drug from one cell type to another. We then construct a combined SARS-CoV-2 and aging interactome using a Steiner tree analysis to connect the differentially expressed genes within a protein-protein interaction network [29, 30]. By intersecting the resulting combined SARS-CoV-2 and aging interactome with the targets of the 300 top ranked FDA approved drugs from the previous analysis, we identify serine/threonine and tyrosine kinases as potential drug targets for therapeutic interventions. Causal structure discovery methods applied to the combined SARS-CoV-2 and aging interactome show that the identified protein kinase inhibitors such as axitinib, dasatinib, pazopanib and sunitinib target proteins that are upstream from genes that are differentially expressed in SARS-CoV-2 infection and aging, thereby validating these drugs as being of particular interest for the repurposing against COVID-19. While we apply our computational platform in the context of SARS-CoV-2, our algorithms integrate data modalities that are available for many diseases, thereby making them broadly applicable.

Results

Differential expression analysis identifies genes that intersect the SARS-CoV-2 host response and aging pathways

Since age is strongly associated with severe outcomes in patients with COVID-19, we sought to analyze genes differentially expressed in normal versus SARS-CoV-2 infected cells as well as genes differentially expressed in young versus old individuals. Used as model system for lung epithelial cells and the effect of SARS-CoV-2 infection, we obtained from [23] RNA-seq samples from normal and SARS-CoV-2 infected A549 lung alveolar cells as well as A549 cells supplemented with ACE2 (A549-ACE2), a receptor that has been shown to be critical for SARS-CoV-2 cell entry [31]. Fig. 2a shows the expression of A549-ACE2 cells infected with SARS-CoV-2 in comparison to normal A549-ACE2 cells, with many genes upregulated as a result of the infection, as expected. Given the availability of A549 data with/without ACE2 and with/without SARS-CoV-2 infection, we removed genes from this initial list of differentially expressed genes that were just ACE2-specific or just SARS-CoV-2 infection-specific to extract a more refined expression pattern of ACE2-mediated SARS-CoV-2 infection (Methods, Fig. 2b). The rationale was to remove genes linked to the response of the ACE2 receptor to signals other than SARS-CoV-2 infection or genes involved in the entry of SARS-CoV-2 into the cell through means other than the ACE2 receptor, which has been shown to be the critical mode of entry in humans [31]. Gene ontology (GO) enrichment analysis revealed enrichment in mitotic cell cycle as the top term, further supporting removal of these genes (Supplementary Fig. S1). The remaining 1926 genes are denoted in red in Fig. 2a,b and used for the subsequent analysis. GO enrichment analysis of these genes revealed that they are significantly enriched in the type I interferon signaling pathway and defense response to virus in addition to other GO terms (Fig. 2c). Next, in order to analyze the link between SARS-CoV-2 infection and aging, we analyzed RNA-seq samples from the lung of different aged individuals collected as part of the Genome

Tissue Expression (GTEx) study [24]. Given the stark increase in case fatality rates of COVID-19 after age 70 [17, 18], we performed a differential expression analysis comparing the youngest group (20-29 years old) and oldest group (70-79 years old), thereby identifying 1923 genes differentially regulated in aging (Fig. 2d, Supplementary Fig. S2). As shown in Fig. 2e, these genes show a significant overlap with the 1926 genes found to be differentially regulated by SARS-CoV-2 (p -value= 0.01999, Fisher’s exact test), thereby confirming results obtained using a different analysis in [32]. Interestingly, these 219 genes that we found to intersect the SARS-CoV-2 infection and aging pathways (Fig. 2e) display concordant changes in gene expression (i.e. the majority of genes is either upregulated or downregulated with SARS-CoV-2 infection and aging) as shown by the \log_2 -fold changes in Fig. 2f and Supplementary Fig. S3a. The association in the directionality of regulation between SARS-CoV-2 infection and aging is statistically significant (p -value $< 2.2 \times 10^{-16}$, Fisher’s exact test), thereby providing further evidence for the interplay of SARS-CoV-2 host response and aging as hypothesized in [21]. Fig. 2g shows the \log_2 -fold changes of the 10 most differentially expressed genes across aging and SARS-CoV-2 infection (based on the sum of their ranks with Supplementary Fig. S3b showing the distribution of the ranks).

Identification of SARS-CoV-2 infection signature in reduced L1000 gene expression space

Next, we focused our analysis on identifying the SARS-CoV-2 transcriptional signature, which we then correlated with the transcriptional signatures of FDA approved drugs in CMap to identify drugs that could revert the effect of SARS-CoV-2 infection. While this analysis resulting in an initial ranking of FDA approved drugs did not take the transcriptional signature of aging into account, aging was a critical component in the final selection of FDA approved drugs described below.

Since gene expression in CMap was quantified using L1000 reduced representation expression profiling [2], which measures gene expression of 1000 representative genes, we first sought to analyze whether these genes sufficiently capture the transcriptional signature of SARS-CoV-2 infection. For this, we intersected the genes measured both by Blanco et al. [23] and CMap [2], resulting in 911 genes. We found a statistically significant overlap between the genes identified as differentially expressed by SARS-CoV-2 infection in Fig. 2 and the L1000 genes (p -value= 7.94×10^{-16} , Fisher’s exact test), thereby providing a rationale for using the CMap database for drug identification in this disease context (Fig. 3a). We thus proceeded to obtain the signature of SARS-CoV-2 infection in the reduced L1000 gene expression space by projecting the RNA-seq data of A549 cells with and without ACE2-receptor and SARS-CoV-2 infection onto the shared 911 genes. The resulting signatures of SARS-CoV-2 infection and ACE2-receptor are visualized using the first two principal components in Fig. 3b. Interestingly, the signature of SARS-CoV-2 infection (indicated by arrows) was aligned across both A549 and A549-ACE2 cells as well as across different levels of infection (MOI of 0.2 and 2), suggesting that the SARS-CoV-2 transcriptional signature was captured robustly by the L1000 genes, thus providing further rationale for using CMap to identify drugs that could reverse the effect of SARS-CoV-2 infection.

Combined autoencoder and synthetic interventions framework to identify drug signatures and rank FDA approved drugs for SARS-CoV-2

Next, we sought to determine transcriptional drug signatures using the CMap database, which includes among other cell lines A549. The data was visualized using Uniform Manifold Approximation and Projection (UMAP) [33] in Supplementary Fig. S4a, showing that the perturbations clustered by cell type and hence the drug signatures were small relative to the differences between cell types. We intersected the perturbations from CMap with a list of FDA approved drugs using Slinky [34], resulting in 759 drugs of which 605 were available for A549. After removing batch effects using k-means clustering (see Methods and Supplementary Fig. S4b), we computed initial signatures of these drugs based on the mean before and after drug perturbation in A549 cells. Fig. 3c shows a selection of drug signatures in relation to the signature of SARS-CoV-2 infection visualized using the top two principal components.

Since the effect of a drug can be cell-type specific [35], this standard approach to computing drug signatures may not allow extrapolating the obtained signatures beyond A549 cells. In order to determine robust drug signatures and consider also FDA approved drugs that have been dosed on cell lines other than A549 in CMap, we employed an autoencoder framework. Autoencoders, a particular class of neural networks where an input is mapped through a latent space to itself, have been widely used for representation learning [25, 26, 36] and more recently also in genomics and single-cell biology [37, 38, 39]. We trained an autoencoder (architecture described in Supplementary Fig. S5) to minimize reconstruction

error on CMap data and data from Blanco et al. [23] in the L1000 gene expression space. We then computed the disease and drug signatures based on the embedding of the data in the latent space. Interestingly, by comparing the correlations between drug signatures obtained from A549 cells and MCF7 cells (Fig. 3d) as well as HCC515 cells (Supplementary Fig. S7), cell lines with many perturbations in CMap, it is apparent that the autoencoder aligned the drug signatures across different cell types. While autoencoders and other generative models have been used for computing signatures of perturbations also in other works [39, 40], these works have used autoencoders in the standard way to obtain a *lower*-dimensional embedding of the data. Motivated by our recent work which, quite counter-intuitively, described various benefits of using autoencoders to learn a latent representation of the data that is *higher*-dimensional than the original space [41], we found that overparameterized autoencoders not only led to better reconstruction of the data than standardly used autoencoders (Supplementary Fig. S6 and architectures described in Supplementary Fig. S5), but also to a better alignment of drug signatures between different cell types (Supplementary Fig. S7). Interestingly, overparameterized autoencoders provided about the same alignment of drug signatures as using the top three principal components (Fig. 3e), while at the same time allowing a near perfect reconstruction of the original gene expression vectors from the embedding. Providing additional validation of the latent space embedding obtained by the overparameterized autoencoder, we found that known ACE2 inhibitors were generally aligned with the reverse signature of ACE2 in A549 cells (e.g. correlations for moexipril, quinapril and perindopril are all 0.88; see Supplementary Dataset 1). We thus used this latent space embedding to rank the drugs based on their correlation with the reverse disease signature in A549 cells (Supplementary Dataset 1). Since overparameterized autoencoders aligned drug signatures across cell types, this embedding also allowed constructing synthetic interventions [27, 28], i.e., to predict the effect of a drug on A549 cells without measuring it, by linearly transferring the corresponding drug signature in the latent space from a cell type where it has been measured. In this way, we obtained an enlarged list of drug signatures, which we correlated in the latent space with the reverse disease signature to obtain further candidates of FDA approved drugs for SARS-CoV-2 (Supplementary Dataset 1). To compare the correlations obtained with the different embeddings, a list of the top ranked drugs is shown in Fig. 3f. Interestingly, it contains various drugs that were identified also in [6] using a different analysis (clemastine, haloperidol, ribavirin) or are currently in clinical trials (ribavirin, quinapril).

Steiner tree analysis identifies candidate drug targets by constructing combined SARS-CoV-2 and aging interactome

Our differential expression analysis revealed relevant genes to investigate in the context of SARS-Cov-2 infection and aging, while the combined autoencoder and synthetic interventions analysis provided candidate FDA approved drugs for reverting the effect of SARS-CoV-2 infection. Next, we integrated these two separate analyses to obtain a final list of FDA approved drugs by constructing a combined SARS-CoV-2 infection and aging protein-protein interactome and intersecting it with the targets of the candidate drugs (Fig. 4a). For this, we selected the differentially expressed genes identified in Fig. 2f that showed concordant regulation between aging and SARS-CoV-2 infection and intersected them with the nodes of the human protein-protein interaction (PPI) network (IRefIndex Version 14 [42]), which contains 182,002 interactions between 15,759 human proteins along with a confidence measure for each interaction. This resulted in 162 protein-coding genes, which we call *terminals* (Supplementary Fig. S8 and Methods). To gain a better understanding of the molecular pathways connecting these terminal genes, we used a Steiner tree algorithm [30, 43] to determine a “minimal” subnetwork or *interactome* within the PPI network that connects these genes (see Methods). A Steiner tree is minimal in that it is a minimum weight subnetwork that connects the terminals. As edge weights in the PPI network we used 1 minus the confidence in the corresponding interactions so as to favor high-confidence edges. After a careful sensitivity analysis to select the various tuning parameters (Methods and Supplementary Fig. S9), this resulted in an interactome containing 252 nodes and 1,003 edges (Fig. 4b and Supplementary Fig. S10). Interestingly, the interactome contained five genes whose corresponding proteins have been found in [6] to interact with SARS-Cov-2 proteins (EXOSC5, FOXRED2, LOX, RBX1, RIPK1). The 2-nearest-neighborhoods of these proteins are shown in Fig. 4c. Another Steiner tree analysis revealed that two additional SARS-Cov-2 interaction partners (CUL2 and HDAC2) were connected to the identified interactome via few high-confidence edges (Supplementary Fig. S11 - S13).

Next, we intersected the interactome with the targets of the candidate drugs identified in the previous analysis. A compound was considered if its signature matched the reverse SARS-CoV-2 signature with at least a correlation of 0.86, resulting in about 300 FDA approved drugs (see Methods). The targets of

these drugs were determined using DrugCentral [44, 45] and filtered for high affinity (activity constants lower than $10\mu M$, a common threshold used in the field for K_i , K_d , IC_{50} or EC_{50}). Interestingly, the resulting drugs, shown in Fig. 4d, consisted (with few exceptions) of protein kinase inhibitors (e.g. axitinib, dasatinib, pazopanib, sunitinib). To analyze the specificity of our findings to SARS-CoV-2 infection in aged individuals, we repeated the above analysis without using the GTEx data. This resulted in an interactome containing 1,052 edges across 270 nodes, 42 of which (15%) were also present in the interactome taking age into consideration (Supplementary Fig. S14). This pure SARS-CoV-2 interactome contained 6 SARS-CoV-2 interaction partners (ETFA, GNB1, NUP62, RBX1, RIPK1, SNIP1). Drugs targeting proteins in this interactome belonged to several families including serotonin inhibitors (clozapine, cyproheptadine, desipramine, methysergide), histamine H1 blockers (clemastine, cyproheptadine, ketotifen), tyrosine kinase inhibitors (including axitinib, dasatinib, pazopanib, sunitinib) and HDAC inhibitors (vorinostat, belinostat). This analysis shows that taking aging into account acted as a valuable filter for the identification of drugs.

Causal structure discovery methods validate serine/threonine and tyrosine kinases as critical targets in SARS-CoV-2 infection in the elderly.

Finally, in order to suggest putative causal drug mechanisms and validate the predicted drugs for COVID-19, we supplemented the PPI analysis with causal structure discovery. Since the edges in the PPI network and hence in the SARS-CoV-2 and aging interactome are undirected, it is a-priori not clear whether a drug that targets a node in the interactome has any effect on the differentially expressed terminal nodes, since the target may be downstream of these nodes (Fig. 5a). To understand which genes can be modulated by a drug, it is therefore critical to obtain a causal (directed) network. We obtained single-cell RNA-seq data for A549 cells from [46] and intersected it with the genes present in the combined SARS-CoV-2 and aging interactome. To learn the (causal) regulatory network among these genes, we took advantage of recently developed causal structure discovery algorithms, in particular the greedy sparsest permutation (GSP) algorithm: it performs a greedy search over orderings of the genes to find the sparsest causal network that best fits the data, and it has been successfully applied to single-cell gene expression data before [11, 12, 47]. To validate the obtained causal model and benchmark the performance of GSP to other prominent causal structure discovery algorithms including PC and GES [48], we took advantage of the gene knockout and overexpression data available from CMap. A causal model should allow predicting the effect of such interventions. Thus, for each such gene knockout and overexpression experiment in CMap that targeted a gene in the interactome, we inferred the genes whose expression changed as a result of the intervention, when compared to control samples (Methods and Supplementary Fig. S15a). We then constructed receiver operating characteristic (ROC) curves to evaluate GSP, PC and GES by varying their tuning parameters and counting an edge $i \rightarrow j$ as a true positive if intervening on gene i resulted in a change in the expression of gene j and a false positive otherwise, thereby showing that GSP exceeded random guessing based on the PPI network (p -value=0.0177, see Methods) and outperformed the other methods (Supplementary Fig. S15b).

Having established that the causal network obtained by GSP can be used to predict the effect of an intervention, we turned to analyzing the regulatory effects of the identified candidate drugs on the SARS-CoV-2 and aging interactome in A549 cells. The main connected component of the corresponding causal graph is shown in Fig. 5a (see also Supplementary Fig. S16a) highlighting the drug targets and the genes that were found to be differentially expressed by SARS-CoV-2 infection and aging. We then traced the possible downstream effects for each identified drug, thereby finding that the protein kinase inhibitors and HDAC inhibitors could target the majority of differentially expressed genes in this connected component (Table S1). Similarly, we traced the downstream effects for each gene in the interactome that can be targeted by one of the identified drugs, thereby finding that EGFR, FGFR3, HDAC1, HSP90AA1, IRAK1, PAK1, RIPK1, RIPK2, STK3 all have downstream nodes in the interactome with RIPK1 having the largest number of them (127). To validate these results in a broader context, we obtained single-cell RNA-seq data from [49] and repeated the analysis in AT2 cells, which have been shown to be critically affected by SARS-CoV-2 in humans [31]. The resulting causal network for AT2 cells (Supplementary Fig. S16b) is similar to the one for A549 cells, intersecting it in 55.3% of the edges, with EGFR, HDAC1, HSP90AA1, IRAK1, RIPK1 and RIPK2 all having descendants in the interactome, and targets of protein kinase inhibitors and HDAC inhibitors being particularly central (Table S1). To analyze the most critical targets for the crosstalk between SARS-CoV-2 and aging, we repeated the analysis in the interactome obtained without taking aging into account (Supplementary Fig. S16c). Interestingly, while HDAC1 and HSP90AA1 continued to have widespread effect, the number of genes downstream of RIPK1 changed

drastically to just 1, suggesting that RIPK1 plays a critical role in the SARS-CoV-2 and aging cross-talk. In line with this, while the effect of HDAC inhibitors remained similar in the analysis without ageing, the effect of protein kinase inhibitors changed drastically (Table S1). Collectively, our combined analysis points to protein kinase inhibitors, and it in particular highlights RIPK1, a serine/threonine-protein kinase, as one of the main targets against SARS-CoV-2 infections with a highly age-dependent role and the largest number of downstream differentially expressed genes in the combined SARS-CoV-2 and ageing interactome.

Discussion

The repurposing of drugs for SARS-CoV-2 has been a major challenge given the many pathways involved in host-pathogen interactions and the intricate interplay of SARS-CoV-2 with inflammatory pathways [14, 13, 15, 16]. Interestingly, while both young and old individuals are susceptible to SARS-CoV-2 infection, the virus' pathogenicity is significantly more pronounced in the elderly [17, 18]. Since the mechanical properties of the lung tissue change with aging [19], this led us to hypothesize an interplay between viral infection/replication and tissue aging [21], suggesting that this could play an important role in drug discovery programs. While ongoing drug repurposing efforts have analyzed host-pathogen interactions and the associated gene expression programs [6, 23], they have lacked an integration with aging. More generally, while a number of data-driven and experimental approaches have been proposed for drug identification and repurposing [1], a platform that systematically integrates different data modalities including transcriptomic, proteomic and structural data into a principled causal framework to predict the effect of different drugs has been missing.

By combining bulk RNA-seq data from GTEx [24] and Blanco et al. [23], we identified a critical group of genes that were differentially expressed by aging and by SARS-CoV-2 infection. While previous analysis relied primarily on contrasting the expression in cells with and without SARS-CoV-2 infection [32], we made an attempt to separate the effect of the ACE2 receptor alone and the effect of SARS-CoV-2 in cells without ACE2 receptor to extract a more refined differential expression pattern of ACE2-mediated SARS-CoV-2 infection. While previous computational efforts to repurpose drugs have mainly considered two approaches: (1) identifying drug targets by analyzing disease networks based for example on PPI or transcriptomic data [5, 4, 6], and (2) identifying drugs by matching their signature (for example obtained from the CMap project [2]) to the reverse disease signature [3], we developed a principled causal framework that encompasses these two approaches. First, in order to ensure that the CMap database, which measures expression using 1000 representative genes, would be useful in the context of SARS-CoV-2, we validated that the intersection of these genes with the SARS-CoV-2 differentially expressed genes was significant. Second, to establish drug signatures based on the CMap database, we employed a particular autoencoder framework [41]. Rather unintuitively, we showed that using an overparameterized autoencoder, i.e. by using an autoencoder not to perform dimension reduction as usual but to instead embed the data into a higher-dimensional space, aligned the drug signatures across different cell types. This allowed constructing synthetic interventions, i.e., to predict the effect of a drug on a cell type without measuring it by using other cell types to infer it. Third, to identify drug targets in the pathways intersecting SARS-CoV-2 and aging, we connected the differentially expressed genes in the PPI network using a Steiner tree analysis [30] and intersected the resulting interactome with high-affinity targets of the drugs obtained using the overparameterized autoencoder framework. Finally, while computational drug discovery programs have been largely correlative [1], we made use of recent causal structure discovery algorithms [11, 47, 48] to validate the identified drug targets and their downstream effects, thereby identifying protein kinase inhibitors such as axitinib, dasatinib, pazopanib, and sunitinib as drugs of particular interest for the repurposing against COVID-19.

Among the various protein kinases, in particular from the family of serine/threonine-protein kinases, identified by our drug repurposing pipeline, RIPK1 was singled out by our causal analysis as being upstream of the largest number of genes that were differentially expressed by SARS-CoV-2 infection and aging, while losing its central role in the corresponding gene regulatory network without taking aging into account. Notably, RIPK1 has been shown to bind to SARS-CoV-2 proteins [6] and has also been found to be in an age-dependent module [32]. RIPK1 belongs to an interesting family of proteins comprising of a kinase domain on the N terminus and a death domain on the C terminus; activation of the kinase domain has been associated with epithelial cell homeostasis, while activation of the death domain leads to triggering necroptotic or apoptotic pathways [50, 51], the death pathways potentially triggering tissue fibrosis [52]. Interestingly, our differential expression analysis found RIPK1 to be upregulated with SARS-COV-2 infection. We hypothesize that upon SARS-CoV-2 infection in older individuals the death

pathways may be favored, thereby leading to fibrosis and increased blood clotting. Consistent with this, recent post-mortem lung tissue biopsies of SARS-CoV-2 human patients revealed a fibrotic epithelium and increased blood clotting [53, 54].

Collectively, these results highlight the importance of RIPK1 in the interplay between SARS-CoV-2 infection and aging as a potential target for drug repurposing programs. There are various drugs currently approved that non-specifically target RIPK1 (such as pazopanib and sunitinib) as well as under investigation that are highly specific to RIPK1 [55, 56]. Given the distinct pathways elicited by RIPK1, there is a need to develop appropriate cell culture models that can differentiate between young and aging tissues to validate our findings experimentally and allow for highly specific and targeted drug discovery programs. While our work identified particular drugs and drug targets in the context of COVID-19, our computational platform is applicable well beyond SARS-CoV-2, and we believe that the integration of transcriptional, proteomic and structural data with network models into a causal framework is an important addition to current drug discovery pipelines.

Methods

Bulk gene expression data

The RNA-seq gene expression data related to SARS-CoV-2 infection in A549 and A549-ACE2 cells was obtained from [23] under accession code GSE147507. The RNA-seq data of lung tissues for the aging analysis was downloaded from the GTEx Portal (<https://gtexportal.org/home/index.html>) along with metadata containing the age of the individual from whom the RNA-seq sample was obtained. The RNA-seq raw read counts were transformed into quantile normalized, $\log_2(x + 1)$ scaled RPKM values, following the normalization performed in [2].

Differential expression analysis

For differential expression analysis, we focused on genes that were highly expressed, filtering out any genes with $\log_2(\text{RPKM} + 1) < 1$ for all considered datasets. In order to determine the ACE2-mediated SARS-CoV-2 genes, we computed three different \log_2 -fold changes based on the data from [23]. Namely, we defined as ACE2-mediated SARS-CoV-2 genes all genes that had an absolute \log_2 -fold change between A549-ACE2 cells infected with SARS-CoV-2 and A549-ACE2 cells above threshold, excluding genes that had an absolute \log_2 -fold change above the same threshold in A549-ACE2 cells versus A549 cells and also excluding genes that had an absolute \log_2 -fold change above the same threshold in A549 cells infected with SARS-CoV-2 versus normal A549 cells. In other words, the ACE2-mediated SARS-CoV-2 genes were defined as the genes denoted in red in the Venn diagram in Fig. 2b (with pink, brown and yellow subsets removed). The absolute \log_2 -fold change threshold was determined such that the number of ACE2-mediated SARS-CoV-2 genes was 10% of the protein coding genes.

In order to determine the age associated genes, we analyzed lung tissue samples obtained from the GTEx portal (<https://gtexportal.org/home/index.html>) from individuals of varying ages. We computed the absolute \log_2 -fold change between samples of the lung tissue from older (70-79 years old) and younger (20-29 years old) individuals, defining the age associated genes as the top 10% of protein coding genes with highest absolute \log_2 -fold change. We also considered defining age-associated genes based on the absolute \log_2 -fold change comparing individuals who are 20-29 years old versus 60-79 years old, which yielded similar age-associated genes, with 1339 out of the 1923 genes in common between the two sets as shown in Supplementary Fig. S2b.

Gene ontology enrichment analysis

Gene ontology analysis was performed on a given gene set using GSEAPy, keeping the top 10 gene ontology biological process terms with lowest p -values. All reported terms had p -values ≤ 0.05 , after adjusting for multiple hypothesis testing using the Benjamini–Hochberg procedure.

L1000 gene expression data from CMap

The CMap data measured via L1000 high-throughput reduced representation expression profiling, which quantifies the expression of 1000 landmark genes, was obtained from [2] under accession code GSE92742.

We chose level 2 data, truncated to only the genes that were also measured by [23], and then performed $\log_2(x + 1)$ scaling and min-max scaling on each of the resulting 911-dimensional expression vectors.

Combined autoencoder and synthetic interventions framework

We first describe our training procedures for the autoencoder framework. CMap contains a total of 1,269,922 gene expression vectors and we performed a 90-10 training-test split resulting in 1,142,929 training examples and 126,993 test examples. We selected the best model by applying early stopping with an upper bound on the number of total epochs being 150. Note that this is well past the usual early stopping method of applying a patience strategy with a patience of at most 10 epochs [57]. All hyperparameter settings, optimizer details, and architecture details are presented in Supplementary Fig. S5c. To summarize, we considered a range of fully connected autoencoders with varying depth, width, and nonlinearity, and we used Adam with a learning rate of 10^{-4} for optimization. To compute the drug signatures via the trained autoencoder, we used as embeddings the output of the first hidden layer prior to application of the activation function.

Drug signatures for the A549 cells (and similarly for the MCF7 and HCC515 cells) in CMap were computed by taking the difference between the mean embedding for the A549 samples with drug and the mean embedding for the A549 control (DMSO) samples. To remove batch effects, we performed k -means clustering of the control samples in the embedding space and removed all points falling in the smaller of the two clusters (see Supplementary Fig. S4b).

Next, we briefly describe the synthetic interventions framework and how the embedding from our trained overparameterized autoencoder is used for this. The traditional application of synthetic interventions [27, 28] in the context of drug repurposing would proceed as follows: when a drug signature is unavailable on a given cell type but is available on other cell types, we would express the cell type as a linear combination of the other cell types and use this linear combination to predict the signature on the cell type for which data is unavailable. Since we demonstrated that over-parameterized autoencoders align drug signatures between different cell types (Supplementary Fig. S7), instead of using a linear combination of drug signatures across cell types, we can simply use one of the available drug signatures as the synthetic intervention. In particular, in this work, we used drug signatures on MCF7 cells to construct synthetic interventions for A549 cells. We also considered drug signatures on HCC515 cells; however, there was only one FDA approved drug that was applied to HCC515 cells which was not also applied to A549 cells in CMap. While this analysis did not help to increase the number of considered drugs, we used the data on HCC515 cells in conjunction with the data on A549 and MCF7 cells to validate that the overparameterized autoencoder aligns the signatures of drugs between different cell types (Fig. 3d and Supplementary Fig. S7).

Cosine similarity between perturbations

For each cell type and perturbation, we computed a cell-type specific “perturbation signature”, which is defined as the difference between the average gene expression of a cell type under that perturbation and under the control perturbation, DMSO. Then, for each perturbation, we computed the cosine similarity $\frac{a \cdot b}{|a||b|}$ between the perturbation vectors for all pairs of cell types which received that perturbation in CMap. For example, daunorubicin was applied to 14 cell types in cMap, resulting in $\binom{14}{2} = 91$ cosine similarities associated with daunorubicin. All cosine similarities were plotted (Fig. 3e).

Steiner tree analysis

Human protein-protein interaction (PPI) network

A weighted version of the publicly available IRefIndex v14 human PPI network [42] was retrieved from the OmicsIntegrator2 GitHub repository (<http://github.com/fraenkel-lab/OmicsIntegrator2>). The interactome contains 182,002 interactions between 15,759 proteins. Each interaction e has an associated cost $c(e) = 1 - m(e)$ where the score $m(e)$ is obtained using the MIScore algorithm [58], which quantifies confidence in the interaction e based on several evidence criteria (e.g. number of publications reporting the interaction and corresponding detection methods).

Human-SARS-Cov-2 PPI network

A high-confidence host-pathogen interaction map of 27 SARS-Cov-2 viral proteins with HEK293T proteins [6] was retrieved from NDEX (<http://www.ndexbio.org/#/network/5d97a04a-6fab-11ea-bfcd-0ac135e8bacf>), which reports interactions with 332 human proteins.

Drug-target interaction data

Data on the targets of drugs was obtained from DrugCentral (<http://drugcentral.org/download>), an online drug information resource, which includes drug-target interaction data extracted from the literature along with metrics (such as inhibition constant K_i , dissociation constant K_d , effective concentration $EC50$, and inhibitory concentration $IC50$) measuring the affinity of the drug for its target [44, 45]. Drugs in the database are approved by the FDA and may also be approved by other regulatory agencies (such as the EMA). From this database, we filtered out compounds targeting non-human proteins. We also discarded drug-target pairs with affinity metrics (K_i , K_d , $EC50$ or $IC50$) higher than $10\mu M$, a commonly used threshold in the field. Based on this filtering we obtained a data set containing 12,949 high affinity drug-target pairs involving 1,457 unique human protein targets and 2,095 unique compounds. This dataset was further restricted to drugs predicted to reverse the SARS-Cov-2 signature (correlation greater than 0.86 in the overparameterized autoencoder embedding). As a result, the final drug-target data set included information on 2,296 drug-target pairs involving 652 unique human gene targets and 117 unique FDA approved drugs.

Prize-collecting Steiner forest algorithm

The Prize-Collecting Steiner Forest (PCSF) problem is an extension of the classical Steiner tree problem: Given a connected undirected network with non-negative edge weights (costs) and a subset of nodes, the *terminals*, find a subnetwork of minimum weight that contains all terminals. The resulting subnetwork is always a tree, which in general contains more nodes than the terminals; these are known as *Steiner nodes*. In the special case when there are only 2 terminals, this boils down to finding the shortest path between these nodes. The Steiner tree problem in general is known to be NP-complete, but various approximations are available. The PCSF problem generalizes this problem by introducing prizes for the terminals (in addition to the edge costs already present in the Steiner tree problem) and a dummy node connected to all terminals. The problem is then to find a connected subnetwork that minimizes an objective function involving the cost of selected edges and the prizes of terminals that are missing from the subnetwork as detailed below; we used OmicsIntegrator2 to solve this optimization problem [30].

To formally introduce the objective function, let $G = (V, E, c(\cdot), p(\cdot))$ denote the undirected PPI network with protein set V (containing N proteins), interaction set E , edge cost function $c(\cdot)$, set of terminals $S \subset V$ (containing N proteins) and attributed prizes $p(\cdot)$. The version of the PCSF problem solved by OmicsIntegrator2 [30] and used in this article consists of finding a connected subnetwork $T = (V_T, E_T)$ of the modified graph $G^* = (V \cup \{r\}, E \cup \{\{r, s\} : s \in S\})$ that minimizes the objective function

$$\psi(T) = b \sum_{v \notin V_T} p(v) + \sum_{e \in E_T} c^*(e)$$

The node r is a dummy root node connecting all terminals in the network. The parameter $b \in \mathbb{R}^+$ linearly scales the node prizes (which are non-zero for terminal nodes exclusively), and the modified edge cost function $c^*(\cdot)$ can be expressed as follows. For any edge $e = \{x, y\}$

$$c^*(e) = \begin{cases} c(e) + \frac{d_x d_y}{d_x d_y + (N - d_x - 1)(N - d_y - 1)} 10^g & \text{if } e \in E \\ w & \text{if } e \in \{\{r, s\} : s \in S\} \end{cases} \quad (1)$$

where d_x denotes the degree of node x in G and $g, w \in \mathbb{R}^+$ are tuning parameters. If the resulting tree contains the root node r , r is removed from the tree, and the output is an ensemble of trees, a *forest*. The final output, the *interactome*, is the subnetwork in the PPI network induced by the nodes of this forest.

Selection of terminal nodes

Results from the differential expression analysis yielded 219 protein-coding genes that were associated with both aging and SARS-Cov-2 infection. Of particular interest among these genes were 181 genes

that showed concordant regulation, i.e. they were either upregulated in both SARS-Cov-2 infection and aging or downregulated in both SARS-Cov-2 infection and aging. Intersecting the proteins corresponding to these 181 genes with proteins in the IREF interactome resulted in 162 proteins. These 162 proteins were selected as terminal nodes for the PCSF algorithm and prized according to their absolute \log_2 -fold change between SARS-Cov-2-infected A549-ACE2 cells and normal A549-ACE2 cells (Supplementary Fig. S8)

Parameter sensitivity analysis

Running the PCSF algorithm in the OmicsIntegrator2 required specifying three tuning parameters: g , w and b . In order to guarantee the robustness of the resulting network with respect to moderate changes in these parameters, we selected the parameters based on a sensitivity analysis.

The parameter g modifies the background PPI network by imposing an additive penalty on each edge based on the degrees of the corresponding vertices. It reduces the propensity of the algorithm to select hub nodes connecting many proteins in the interactome. While this feature may be relevant in certain biological applications, it was not necessarily the case in our work since high degree nodes may be of interest for the purpose of drug target identification. In the cost function in Equation (1), the absence of penalty corresponds to $g = -\infty$. However the OmicsIntegrator2 implementation only allows for $g \in \mathbb{R}^+$. In Supplementary Fig. S9a1, we reported boxplots of penalized edge costs in the IREF interactome for different values of g . These boxplots suggest that the hub penalty parameter $g = 0$ yields similar edge costs to the desired setting where $g = -\infty$. For this reason we chose the value $g = 0$ in all OmicsIntegrator2 runs in this work.

The parameter w corresponds to the cost of edges connecting terminal nodes to the dummy root r . This parameter influences the number of trees in the Steiner forest. If w is chosen too low compared to the typical shortest path cost between two terminals, a trivial solution will connect all terminal nodes via r , leading to fully isolated terminals in the final forest. For high values of w the PCSF algorithm will not include the root r and output a connected network. Based on the histogram of the cost of the shortest path between any two terminals in the IREF interactome reported in Supplementary Fig. S9a2, we ran a sensitivity analysis for w in the range $[0.2, 2]$.

The parameter b linearly inflates the prizes of terminal nodes in the objective function. Higher values of b result in more terminal nodes in the final PCSF. We analyzed edge costs in the network to determine a suitable range for b so as to include many terminal nodes in the resulting interactome. Supplementary Fig. S9a1 shows that the maximum edge cost in the network for $g = 0$ was lower than 1, which meant that making b of order greater than 1 was necessary to ensure that trading off cost of edges added and prizes collected in the solution would rarely require discarding a terminal node. For this reason we ran a sensitivity analysis for b in the range $[5, 50]$.

Based on the previous considerations we fixed $g = 0$ and ran a sensitivity analysis as described in Supplementary Fig. S9b with $w \in \{0.2, 0.4, 0.6, 0.8, 1, 1.2, 1.4, 1.6, 1.8, 2\}$ and $b \in \{5, 10, 15, 20, 25, 30, 35, 40, 45, 50\}$. We obtained 100 PCSFs, each corresponding to a particular choice of (w, b) . All of them included the entire terminal set S , a desired property resulting from the chosen range of the values of b . To analyze the robustness of the resulting networks to changes in the parameters, we analyzed the matrix $M \in [0, 1]^{100 \times 100}$ defined by

$$M_{ij} = \frac{|\{\text{nodes in } i\} \cap \{\text{nodes in } j\} \cap \mathcal{C}|}{|(\{\text{nodes in } i\} \cup \{\text{nodes in } j\}) \cap \mathcal{C}|}$$

for every pair of PCSFs i and j corresponding to parameters (w_i, b_i) and (w_j, b_j) , respectively. Supplementary Fig. S9c displays heatmaps of this matrix. We considered three different node sets \mathcal{C} , namely the set of all nodes in the input PPI network (Supplementary Fig. S9c1), the subset of terminal nodes ($\mathcal{C} = S$, Supplementary Fig. S9c2) and the subset of SARS-Cov-2 interaction partners (Supplementary Fig. S9c3). Supplementary Fig. S9c1, S9c2, S9c3 illustrate that choosing any $(w, b) \in [1.2, 2] \times [5, 50]$ led to the same connected PCSF with 252 nodes and 1,003 edges. This network is robust to moderate parameter changes for w and b . Collectively, this sensitivity analysis motivated the choice of $g = 0$, $w = 1.4$ and $b = 40$ used to obtain the interactome in Fig. 4b, where nodes are grouped by general function. The same interactome is presented in Supplementary Fig. S10 with nodes grouped by general process. Note that since this interactome included all terminals and did not include the root node, it is equivalent to the solution of the classical Steiner tree problem.

Neighborhood analysis

For the interactomes obtained in this work, we reported 2-nearest-neighborhoods of genes of interest in Fig. 4c for the interactome of Fig. 4b, in Supplementary Fig. S13 for the interactome of Supplementary Fig. S12, and in Supplementary Fig. S14d for the interactome in Supplementary Fig. S14c. Depending on the interactome, genes of interest include SARS-Cov-2 interaction partners (e.g. EXOSC5, FOXRED2, LOX, RBX1, RIPK1) as well as genes of potential therapeutic interest (e.g. HDAC1, EGFR). Neighborhood plots were enriched with information such as SARS-Cov-2 interaction partners and FDA approved, high affinity (based on data from DrugCentral) drugs with high correlation to the reverse SARS-Cov-2 infection signature. To improve legibility of the neighborhood networks, we discarded the highly connected hub node UBC (connected to 62% of proteins in the IREF network). To further improve legibility, we applied an upper threshold on edge cost (i.e., only visualizing high confidence edges) when the neighborhood networks were too densely connected. We generally chose this threshold at 0.53, with the exception of the LOX neighborhood (0.58) and the FOXRED2, ETFA and GNB1 neighborhoods (no thresholding). For each edge e in a given neighborhood, we defined the min-max scaled edge confidence $C(e)$ as

$$C(e) = \frac{\max_{e' \in \mathcal{E}} c(e') - c(e)}{\max_{e' \in \mathcal{E}} c(e') - \min_{e' \in \mathcal{E}} c(e')} \in [0, 1]$$

where \mathcal{E} denotes the edge set of the corresponding interactome and $c(e)$ denotes the cost of edge e in the PPI network. This confidence metric was used to color edges in the neighborhood plots.

Addition of SARS-Cov-2 interaction partners to the terminal node list

In order to understand which other SARS-CoV-2 protein interaction partners were in the neighborhood of the identified interactome, we also ran the PCSF algorithm on the IREF PPI network using the SARS-Cov-2 and aging terminal list augmented with all known SARS-Cov-2 interaction partners. All SARS-Cov-2 interaction partners (with the exception of EXOSC5, FOXRED2 and LOX which were already present in the original terminal gene list) were given a small prize p . This prize was chosen by sensitivity analysis over a range of possible values from $p = 0$ (5 SARS-Cov-2 interaction partners initially selected by the method: EXOSC5, FOXRED2, LOX, RBXL1, RIPK1) to $p = 0.02$, beyond which all 332 known SARS-Cov-2 interaction partners belonged to the computed interactome. Fine-grained analysis revealed that choosing $p \in [4 \times 10^{-4}, 10^{-3}]$ leads to interactomes which include a stable set of 7 SARS-Cov-2 interaction partners, the 5 present initially plus CUL2 and HDAC2 (Supplementary Fig. S11a). Supplementary Fig. S11b-S11c display heatmaps of the matrix $M \in [0, 1]^{16 \times 16}$ defined as

$$M_{ij} = \frac{|(\{\text{nodes in } i\} \setminus \{\text{nodes in } j\}) \cap \mathcal{C}|}{|\{\text{nodes in } i\} \cap \mathcal{C}|}$$

for every pair of PCSFs i and j corresponding to parameters p_i and p_j , respectively. For the sensitivity analysis, we considered two different node sets \mathcal{C} , namely the set of all nodes in the input PPI network (Supplementary Fig. S11b) as well as the subset of SARS-Cov-2 interaction partners (Supplementary Fig. S11c). Supplementary Fig. S11b shows that the obtained interactome was stable over the range $p \in [7 \times 10^{-4}, 10^{-3}]$. Supplementary Fig. S11c shows that all SARS-Cov-2 interaction partners collected in the interactome when $p \in [7 \times 10^{-4}, 10^{-3}]$ were also collected for higher values of p , which is a consequence of the observation from Supplementary Fig. S11b. We used the value $p = 8 \times 10^{-4}$ for all subsequent analyses and figures, including Supplementary Fig. S12 and Supplementary Fig. S13.

Single-cell RNA-seq analysis

Single-cell RNA-seq for A549 cells was obtained from GSE81861 [46], where each entry in the matrix represents the gene expression (FPKM) of gene i in cell j . We preprocessed the data, keeping only genes that had a nonzero gene expression value in more than 10% of the cells, followed by $\log_2(x + 1)$ transformation of the data. Single-cell RNA-seq data for AT2 cells was obtained from <http://www.nupulmonary.org/resources> associated with [49]. In order to avoid batch effects, we subset the data to include cells only from Donor 7 since that donor had the largest number of AT2 cells collected (4002 cells). We preprocessed the data using the same threshold as for A549 cells for filtering out genes across cells. Since single-cell RNA-seq data for AT2 cells was not yet normalized, we normalized the expression values across genes for each cell by the total RNA count for that cell, followed by $\log_2(x + 1)$ transformation of the data as for A549 cells.

Evaluation of causal structure discovery algorithms

Prior to reporting the results of learning gene regulatory networks on A549 and AT2 cells, we benchmarked several causal structure discovery methods on the task of predicting the effects of interventions using gene knockout and overexpression data collected on A549 cells as part of the CMap project [2], similar to prior evaluations of causal methods [11, 12]. We estimated the gene regulatory network underlying the identified interactome in A549 cells using the prominent causal structure discovery methods PC, GES and GSP [8, 48, 47]. Since not all edge directions are identifiable from purely observational data, these methods output a causal graph containing both directed and undirected edges. Since the advantage of causal networks is their ability to predict the effects of interventions on downstream genes, we evaluated these methods using interventions collected in CMap. In the following, we first describe how we estimated the effects of interventions based on the CMap data to use as ground truth for evaluating causal structure discovery methods. We focused our evaluation on genes and interventions that are shared between the combined SARS-CoV-2 and aging interactome and CMap knockout and overexpression experiments, resulting in 32 genes and 41 interventions (note that the number of interventions is larger than the number of genes, since in CMap interventions have been performed on genes that are not part of the L1000 landmark genes, but are contained in the interactome). We formed a matrix of genes by interventions, where each (i, j) -entry in the matrix represents the \log_2 -fold change in expression of gene i when gene j was intervened on in comparison to the expression of gene i without intervention. We denoted by Q the binary matrix of intervention effects with $Q_{ij} = 1$ if the sign of the \log_2 -fold change for the (i, j) entry was opposite for knockout and overexpression interventions to filter out unsuccessful interventions, the rationale being that knockout and overexpression should have opposite downstream effects. Thus $Q_{ij} = 1$ denotes that perturbing gene j affects gene i and hence that gene i is downstream of gene j (Supplementary Fig. S15a). Taking this matrix of interventional effects, Q , as the ground truth, we estimated the causal graph using the PC, GES and GSP algorithms and determined the corresponding ROC curve, counting and edge from $j \rightarrow i$ as a true positive if $Q_{ij} = 1$ and a false positive otherwise (Supplementary Fig. S15b). In order to statistically evaluate whether the different algorithms performed better than random guessing, we sampled causal graphs (from an Erdős-Renyi model, where the edges were directed based on a uniformly sampled permutation) with different edge probabilities from the PPI network and calculated the corresponding number of true and false positives. For each false positive level, we created a distribution over true positives based on the sampled random causal graphs and calculated the p -value for the number of true positives obtained from the PC, GES and GSP algorithms. We combined the p -values across different numbers of false positives using Fisher’s method and used this combined p -value for evaluating whether the PC, GES and GSP algorithms were significantly different from random guessing.

Causal structure discovery for learning gene regulatory networks

In order to learn the gene regulatory networks governing A549 and AT2 cells, we used the recent structure discovery method GSP [47, 11, 12] on single-cell RNA-seq data from A549 cells as well as AT2 cells with the PPI network on 252 nodes as a prior. We used GSP since based on the previous analysis it outperformed the PC and GES algorithms in terms of ROC analysis on predicting the effect of gene knockout and overexpression experiments in A549 cells (p -value = 0.0177 for GSP, p -value = 0.0694 for GSP and p -value = 0.5867 for GES); in addition, GSP is also preferable from a theoretical standpoint, since it is consistent under strictly weaker assumptions than the PC and GES algorithms [47]. To obtain an estimate of the causal graph that is robust across hyperparameters and data subsampling, we used stability selection [59]. In short, stability selection estimates the probability of selection of each edge by running GSP on subsamples of the data. Aggregating selection probabilities across algorithm hyperparameters (in this case the α -level for conditional independence testing), edges with high selection probability (0.3 for A549 cells and 0.4 for AT2 cells) were retained. The threshold for AT2 cells was chosen so as to approximately match the number of edges in the A549 network.

Data and code availability

All data used in this work is publicly available from the sources mentioned. We relied on open source code for the analysis (including OmicsIntegrator2, the R package pcalg, as well as the python packages causal DAG, GSEAPy, networkx, numpy, pandas, PyTorch, scikit-learn, scipy). A comprehensive GitHub repository containing all data and code will be made available upon publication of the manuscript.

References

- [1] Pushpakom, S. *et al.* Drug repurposing: progress, challenges and recommendations. *Nature Reviews Drug Discovery* **18**, 41–58 (2019).
- [2] Subramanian, A., Narayan, R., Corsello, S. M. *et al.* A next generation connectivity map: L1000 platform and the first 1,000,000 profiles. *Cell* **171**, 1437–1452.e1 (2017).
- [3] Dudley, J. T., Deshpande, T. & Butte, A. T. Exploiting drug–disease relationships for computational drug repositioning. *Briefings in Bioinformatics* **12**, 303–311 (2011).
- [4] Greene, C. S. & Voight, B. F. Pathway and network-based strategies to translate genetic discoveries into effective therapies. *Human Molecular Genetics* **25**, R94–R98 (2016).
- [5] Smith, S. B., Dampier, W., Tozeren, A., Brown, J. R. & Magid-Slav, M. Identification of common biological pathways and drug targets across multiple respiratory viruses based on human host gene expression analysis. *PLoS One* **7**, e331741 (2012).
- [6] Gordon, D. E. *et al.* A sars-cov-2 protein interaction map reveals targets for drug repurposing. *Nature* (2020).
- [7] Pearl, J. *Causality* (Cambridge University Press, Cambridge, UK, 2009), 2 edn.
- [8] Spirtes, P., Glymour, C. & Scheines, R. *Causation, Prediction, and Search* (MIT press, 2000).
- [9] Eberhardt, F. *Causation and Intervention* (PhD thesis, Department of Philosophy, Carnegie Mellon University, 2007).
- [10] Meinshausen, N. *et al.* Methods for causal inference from gene perturbation experiments and validation. *Proceedings of the National Academy of Sciences, U.S.A.* **113**, 7361–7368 (2016).
- [11] Wang, Y., Solus, L., Yang, K. D. & Uhler, C. Permutation-based causal inference algorithms with interventions. *Advances in Neural Information Processing Systems* **30** (2017).
- [12] Yang, K. D., Katcoff, A. & Uhler, C. Characterizing and learning equivalence classes of causal dags under interventions. *Proceedings of Machine Learning Research* **80**, 5537–5546 (2017).
- [13] de Wit, E., van Doremalen, N., Falzarano, D. & Munster, V. J. Sars and mers: recent insights into emerging coronaviruses. *Nature Reviews Microbiology* **14**, 523 (2016).
- [14] Fung, T. S. & Liu, D. X. Human coronavirus: Host-pathogen interaction. *Annual Review of Microbiology* **73**, 529–557 (2019).
- [15] Poppe, M. *et al.* The nf- κ b-dependent and-independent transcriptome and chromatin landscapes of human coronavirus 229e-infected cells. *PLoS Pathogens* **13**, e1006286 (2017).
- [16] Yang, C. W. *et al.* Targeting coronaviral replication and cellular jak2 mediated dominant nf- κ b activation for comprehensive and ultimate inhibition of coronaviral activity. *Scientific Reports* **7**, 4105 (2017).
- [17] Wu, J. T. *et al.* Estimating clinical severity of COVID-19 from the transmission dynamics in Wuhan, China. *Nature Medicine* **26**, 506–510 (2020).
- [18] Onder, G., Rezza, G. & Brusaferro, S. Case-fatality rate and characteristics of patients dying in relation to COVID-19 in Italy. *JAMA* **323**, 1775–1776 (2020).
- [19] Sicard, D. *et al.* Aging and anatomical variations in lung tissue stiffness. *American Journal of Physiology-Lung Cellular and Molecular Physiology* **314**, L946–L955 (2018).
- [20] Mitra, A. *et al.* Cell geometry dictates TNF α -induced genome response. *Proceedings of the National Academy of Sciences, U.S.A.* **114**, E3882–E3891 (2017).
- [21] Uhler, C. & Shivashankar, G. V. Mechano-genomic regulation of coronaviruses and its interplay with ageing. *Nature Reviews Molecular Cell Biology* **21**, 247–248 (2020).

- [22] Zhou, Y. *et al.* Network-based drug repurposing for novel coronavirus 2019-ncov/sars-cov-2. *Cell Discovery* **6**, 14 (2020).
- [23] Blanco-Melo, D. *et al.* Imbalanced host response to sars-cov-2 drives development of covid-19. *Cell* (2020).
- [24] Carithers, L. J., Ardlie, K., Barcus, M., Branton, P. A. *et al.* A novel approach to high-quality postmortem tissue procurement: the gtex project. *Biopreservation and Biobanking* **13**, 311–319 (2015).
- [25] Baldi, P. Autoencoders, unsupervised learning, and deep architectures. In Guyon, I., Dror, G., Lemaire, V., Taylor, G. & Silver, D. (eds.) *Proceedings of ICML Workshop on Unsupervised and Transfer Learning*, vol. 27 of *Proceedings of Machine Learning Research*, 37–49 (PMLR, Bellevue, Washington, USA, 2012).
- [26] LeCun, Y., Bengio, Y. & Hinton, G. Deep learning. *Nature* **521**, 436–444 (2015).
- [27] Agarwal, A., Cosson, R., Shah, D. & Shen, D. Synthetic interventions. In *Proceedings of CausalML NeurIPS Workshop* (2019).
- [28] Abadie, A., Diamond, A. & Hainmueller, J. Synthetic control methods for comparative case studies: Estimating the effect of california’s tobacco control program. *Journal of the American Statistical Association* **105**, 493–505 (2010).
- [29] De Las Rivas, J. & Fontanillo, C. Protein–protein interactions essentials: Key concepts to building and analyzing interactome networks. *PLoS Computational Biology* **6**, e1000807 (2010).
- [30] Huang, S. S. & Fraenkel, E. Integrating proteomic, transcriptional, and interactome data reveals hidden components of signaling and regulatory networks. *Science Signaling* **2**, ra40 (2009).
- [31] Hoffmann, M. *et al.* SARS-CoV-2 cell entry depends on ACE2 and TMPRSS2 and is blocked by a clinically proven protease inhibitor. *Cell* **181**, 271–280.e8 (2020).
- [32] Chow, R. D. & Chen, S. The aging transcriptome and cellular landscape of the human lung in relation to SARS-CoV-2. <https://doi.org/10.1101/2020.04.07.030684> (2020).
- [33] McInnes, L., Healy, J. & Melville, J. Umap: Uniform manifold approximation and projection for dimension reduction. *arXiv preprint arXiv:1802.03426* (2018).
- [34] Kort, E. J. & Jovinge, S. Streamlined analysis of lincs l1000 data with the slinky package for r. *Bioinformatics* **35**, 3176–3177 (2019).
- [35] Niepel, M. *et al.* Common and cell-type specific responses to anti-cancer drugs revealed by high throughput transcript profiling. *Nature Communications* **8**, 1186 (2017).
- [36] Hinton, G. E. & Salakhutdinov, R. R. Reducing the dimensionality of data with neural networks. *Science* **313**, 504–507 (2006).
- [37] Yang, K. D. *et al.* Autoencoder and optimal transport to infer single-cell trajectories of biological processes. *PLoS Computational Biology* **16**, e1007828 (2020).
- [38] Yang, K. D. *et al.* Multi-domain translation between single-cell imaging and sequencing data using autoencoders. *bioRxiv*, <https://doi.org/10.1101/2019.12.13.875922> (2019).
- [39] Lotfollahi, M., Wolf, F. A. & Theis, F. J. scGen predicts single-cell perturbation responses. *Nature Methods* **16**, 715–721 (2019).
- [40] Ghahramani, A., Watt, F. M. & Luscombe, N. M. Generative adversarial networks simulate gene expression and predict perturbations in single cells. *bioRxiv*, <https://doi.org/10.1101/262501> (2018).
- [41] Radhakrishnan, A., Belkin, M. & Uhler, C. Overparameterized neural networks can implement associative memory. *arXiv:1909.12362* (2019).
- [42] Razick, S., Magklaras, G. & Donaldson, I. M. irefindex: a consolidated protein interaction database with provenance. *BMC Bioinformatics* **9**, 405 (2008).

- [43] Tuncbag, N., McCallum, S., Huang, S. & Fraenkel, E. Steinernet: A web server for integrating ‘omic’ data to discover hidden components of response pathways. *Nucleic Acids Research* (2012).
- [44] Ursu, O. *et al.* Drugcentral: online drug compendium. *Nucleic Acids Research* gkw993 (2016).
- [45] Ursu, O. *et al.* Drugcentral 2018: an update. *Nucleic acids research* **47**, D963–D970 (2019).
- [46] Li, H. *et al.* Reference component analysis of single-cell transcriptomes elucidates cellular heterogeneity in human colorectal tumors. *Nature Genetics* **49**, 708 (2017).
- [47] Solus, L., Wang, Y. & Uhler, C. Consistency guarantees for greedy permutation-based causal inference algorithms. *arXiv:1702.03530* (2017).
- [48] Glymour, C., Zhang, K. & Spirtes, P. Review of causal discovery methods based on graphical models. *Frontiers in Genetics* **10**, 524 (2019).
- [49] Reyfman, P. A. *et al.* Single-cell transcriptomic analysis of human lung provides insights into the pathobiology of pulmonary fibrosis. *American Journal of Respiratory and Critical Care Medicine* **199**, 1517–1536 (2019).
- [50] Festjens, N., Berghe, T. V., Cornelis, S. & Vandenabeele, P. RIP1, a kinase on the crossroads of a cell’s decision to live or die. *Cell Death & Differentiation* **14**, 400–410 (2007).
- [51] Dannappel, M. *et al.* RIPK1 maintains epithelial homeostasis by inhibiting apoptosis and necroptosis. *Nature* **513**, 90–94 (2014).
- [52] Sauler, M., Bazan, I. S. & Lee, P. J. Cell death in the lung: the apoptosis–necroptosis axis. *Annual Review of Physiology* **81**, 375–402 (2019).
- [53] Jose, R. J. & Manuel, A. COVID-19 cytokine storm: the interplay between inflammation and coagulation. *The Lancet Respiratory Medicine* (2020).
- [54] Spagnolo, P. *et al.* Pulmonary fibrosis secondary to COVID-19: a call to arms? *The Lancet Respiratory Medicine* (2020).
- [55] Martens, S., Hofmans, S., Declercq, W., Augustyns, K. & Vandenabeele, P. Inhibitors targeting RIPK1/RIPK3: Old and new drugs. *Trends in Pharmacological Sciences* **41**, 209–224 (2020).
- [56] Degterev, A., Ofengeim, D. & Yuan, J. Targeting RIPK1 for the treatment of human diseases. *Proceedings of the National Academy of Sciences, U.S.A* **116**, 9714–9722 (2019).
- [57] Goodfellow, I., Bengio, Y. & Courville, A. *Deep Learning*, vol. 1 (MIT Press, 2016).
- [58] Kedaigle, A. J. *Integrating Omics data: a new software tool and its use in implicating therapeutic targets in Huntington’s disease*. Ph.D. thesis, Massachusetts Institute of Technology (2018).
- [59] Meinshausen, N. & Bühlmann, P. Stability selection. *Journal of the Royal Statistical Society: Series B (Statistical Methodology)* **72**, 417–473 (2010).

Acknowledgments

A.B. was supported by J-WAFS and J-Clinic for Machine Learning and Health at MIT. A.R. was supported by the National Science Foundation (DMS-1651995) and IBM. C.S. and K.D.Y. were supported by the National Science Foundation (NSF) Graduate Research Fellowships and ONR (N00014-18-1-2765 and N00014-18-1-2765). G.V.S. was supported by ETH funding. C.U. was partially supported by NSF (DMS-1651995), ONR (N00014-17-1-2147 and N00014-18-1-2765), IBM, and a Simons Investigator Award. The Titan Xp used for this research was donated by the NVIDIA Corporation.

Author Contributions

All authors designed the research. A.B., L.C., A.R., C.S. and K.D.Y. developed and implemented the algorithms and performed model and data analysis. A.B., L.C., A.R., G.V.S. and C.U. wrote the paper.

Competing Interests

The authors declare no competing interests.

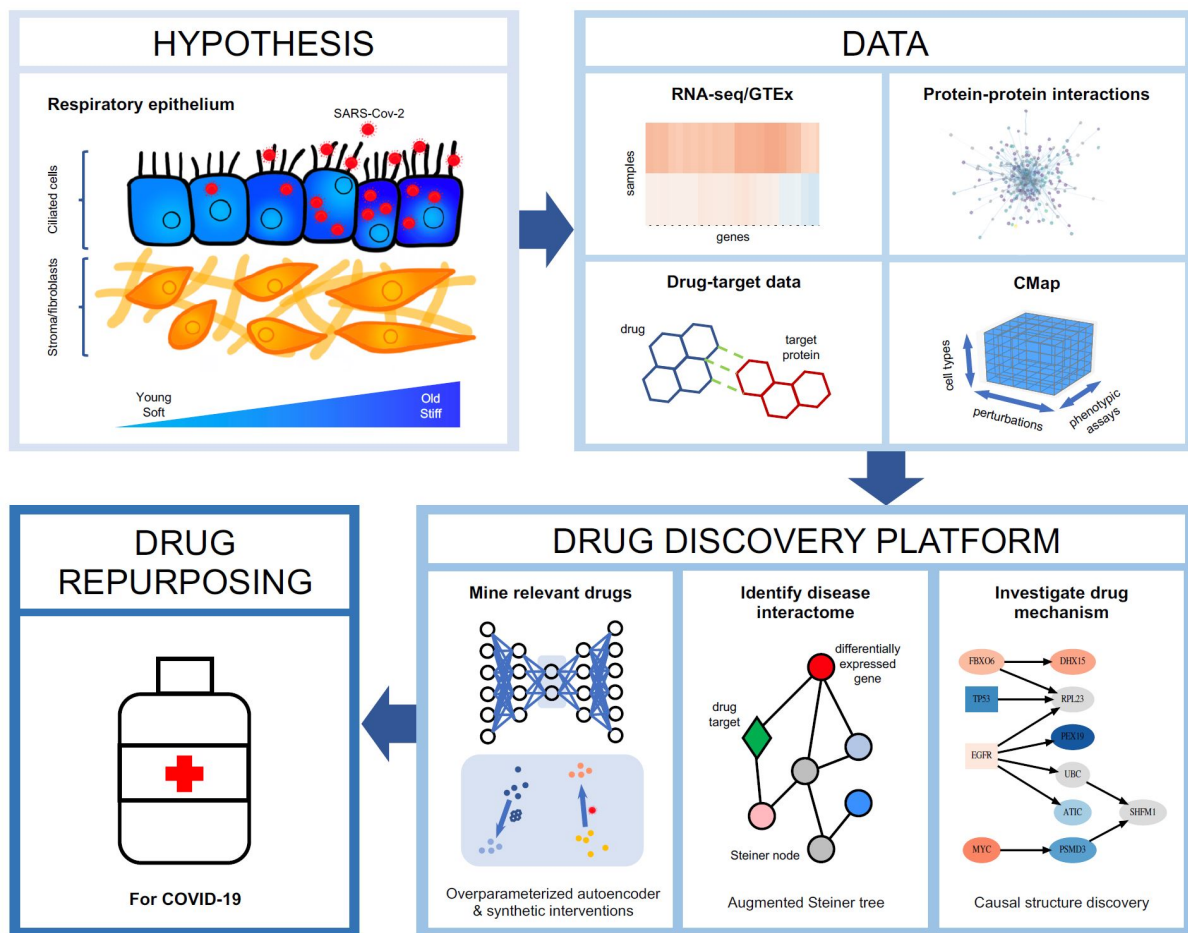


Figure 1: Overview of computational drug repurposing platform for COVID-19. (a) COVID-19 is associated with more severe outcomes in older individuals, suggesting that gene expression programs associated with SARS-CoV-2 and aging must be analyzed in tandem. A potential hypothesis regarding the cross-talk between SARS-CoV-2 and aging relies on changes in tissue stiffness in older individuals, outlined in [21]. (b) In order to identify potential drug candidates for COVID-19, we integrated RNA-seq data from SARS-CoV-2 infected cells (obtained from [23]) and RNA-seq data from the lung tissue of young and old individuals (collected as part of the GTEx project [24]) with protein-protein interaction data (from [42]), drug-target data (from DrugCentral [45]) and the large-scale transcriptional drug screen CMap [2]. (c) Based on this data, we develop a novel drug repurposing pipeline, which consists of first, mining relevant drugs by matching their signatures with the disease signature in the latent embedding obtained by an overparameterized autoencoder and sharing data across cell types to obtain missing drug signatures via synthetic interventions. Second, we identify a disease interactome within the protein-protein interaction network by identifying a minimal subnetwork that connects the genes differentially expressed by SARS-CoV-2 infection and aging using a Steiner tree analysis. Third, we validate the drugs identified in the first step that have targets in the interactome by identifying the potential drug mechanism using causal structure discovery.

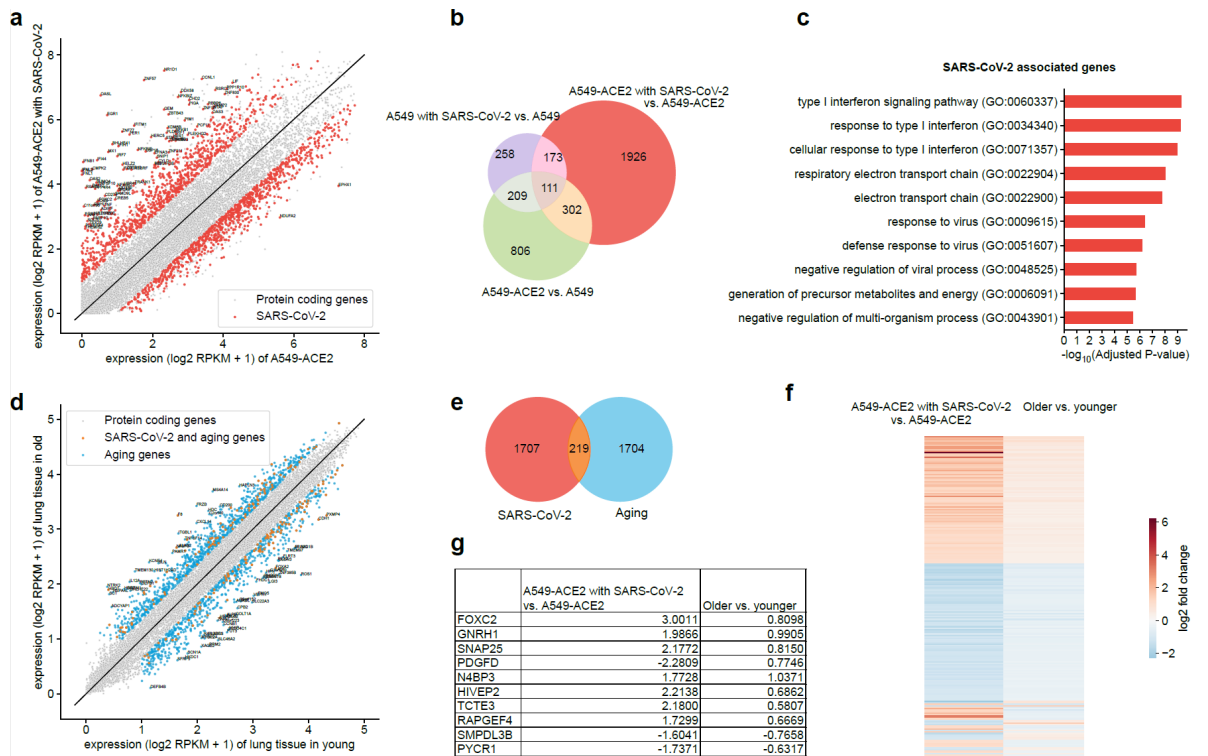


Figure 2: Identification of differentially regulated genes in SARS-CoV-2 infection and aging. (a) Gene expression (\log_2 RPKM + 1) of A549-ACE2 cells infected with SARS-CoV-2 versus normal A549-ACE2 cells. Genes associated with ACE2-mediated SARS-CoV-2 infection after removing just ACE2-specific or just SARS-CoV-2 infection-specific genes are shown in red. (b) Venn diagram, showing the number of genes in sets considered for obtaining the 1926 genes in the red subset and shown in red in (a) associated with ACE-2 mediated SARS-Cov-2 infection. (c) Top 10 gene ontology terms associated with SARS-CoV-2 infection (adjusted p -value < 0.05). (d) Gene expression (\log_2 RPKM + 1) of cells collected from lung tissue of older (70-79 years old) versus younger (20-29 years old) individuals. Differentially expressed genes associated with aging are shown in blue and genes that are associated with both aging and SARS-CoV-2 are shown in orange. (e) Venn diagram of genes associated with SARS-CoV-2 and aging; intersection is significant (p -value = 0.01999, Fisher's exact test). (f) Heatmap of \log_2 -fold changes of differentially expressed genes shared by SARS-CoV-2 and aging; most genes show concordant expression, i.e., they are both upregulated or both downregulated with SARS-CoV-2 infection and ageing. (g) Table of the top 10 most differentially expressed genes across aging and SARS-CoV-2, based on the sum of their ranks with \log_2 -fold changes for each gene.

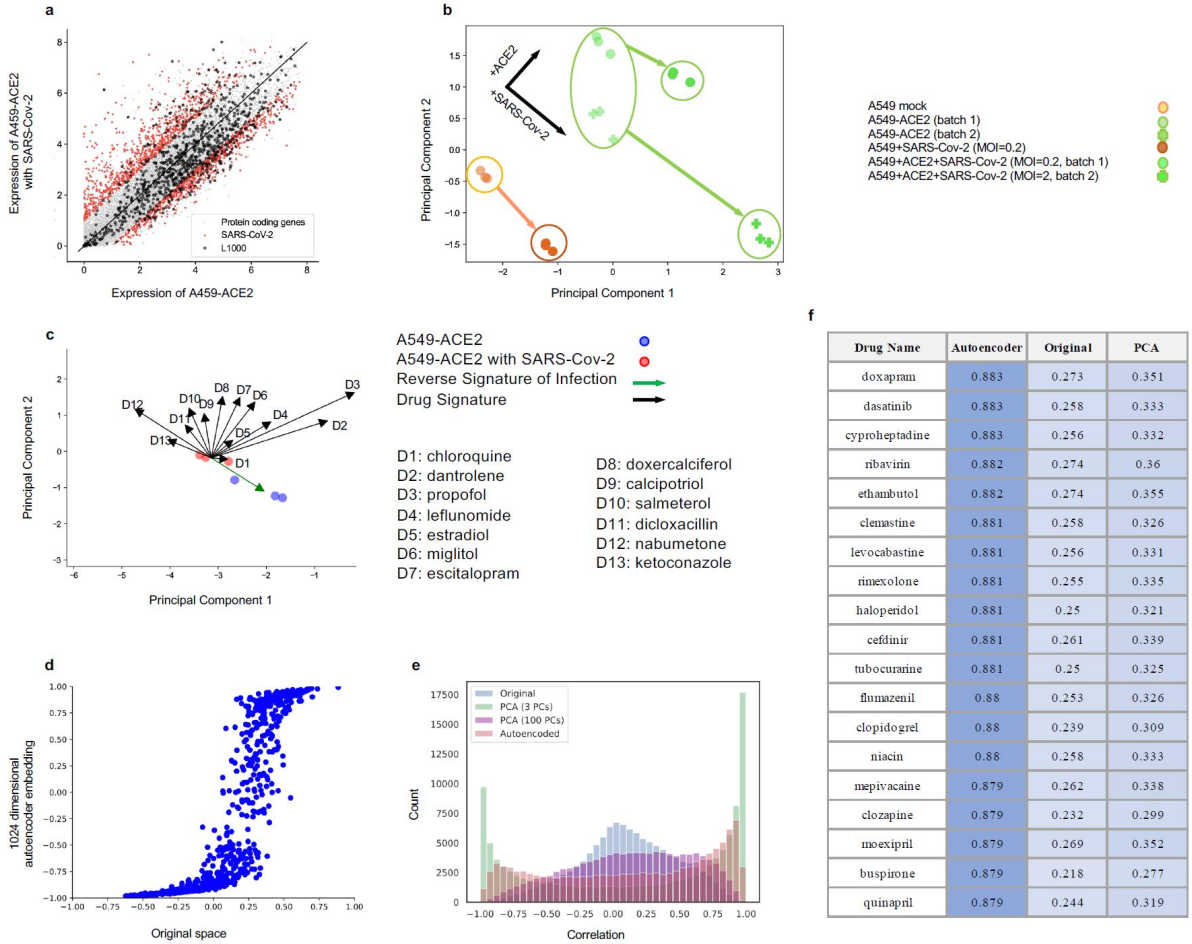


Figure 3: Mining FDA approved drugs by correlating disease and drug signatures using an overparameterized autoencoder embedding. (a) Gene expression (\log_2 RPKM + 1) of A549-ACE2 cells infected with SARS-CoV-2 versus normal A549-ACE2 cells with genes collected as part of the CMap study using L1000 reduced representation expression profiling method highlighted as stars, showing that L1000 genes significantly overlap with SARS-CoV-2 associated genes (p -value= 7.94×10^{-16} , Fisher's exact test). (b) Signature of SARS-CoV-2 infection on A549 and A549-ACE2 cells visualized using the first two principal components based on RNA-seq data from [23]. Signature of SARS-CoV-2 infection is aligned across normal A549 and A549-ACE2 cells as well as across different levels of infection. (c) Comparison of the signatures of a selection of 13 representative FDA approved drugs as compared to the signature of SARS-CoV-2 infection based on A549-ACE2 cells visualized using the first two principal components. Drugs whose signatures maximally align with the direction from SARS-CoV-2 infection to normal are considered candidates for treatment. As expected, drugs have varying signatures of varying magnitudes. (d) Correlation between drug signatures in A549 and MCF7 cells when using the original L1000 expression space versus the embedding obtained from an overparameterized autoencoder. The overparameterized autoencoder aligns the drug signatures in A549 and MCF7 cells by shifting the correlations towards -1 or 1 while maintaining the sign of the correlation in the original space. (e) Histogram of correlations between cell types for a given drug using original L1000 gene expression vectors, overparameterized autoencoder embedding, top 100 principal components, and top 3 principal components. The overparameterized autoencoder achieves about the same alignment of drug signatures as using the top 3 principal components, while at the same time faithfully reconstructing the data (10^{-7} training error). (f) A list of drugs whose signatures maximally align with the direction from SARS-CoV-2 infection to normal in A549-ACE2 cells (MOI 2) with respect to correlations using the overparameterized autoencoder embedding, the original L1000 gene expression space, and the top 100 principal components.

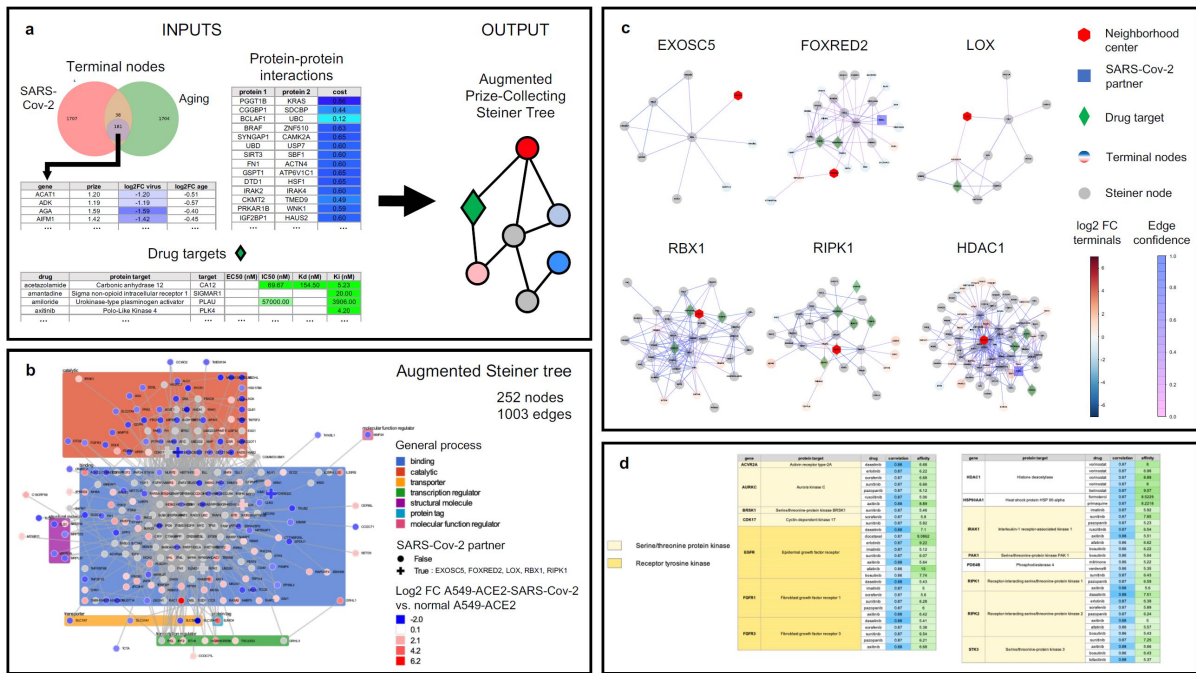


Figure 4: Drug target discovery via Steiner tree analysis to identify putative molecular pathways linking differentially expressed genes in SARS-Cov-2 infection and aging. (a) The general procedure takes as input a list of genes of interest (terminal nodes) with prizes indicating their respective importance, a protein-protein interaction (PPI) network with edge cost/confidence information (e.g. from IRefIndex v14 [42]), and a list of drugs of interest along with their protein targets and available affinity constants (e.g. from DrugCentral [44, 45]). In this study we consider 181 terminal nodes (of which 162 are present in the IREF network) corresponding to genes differentially expressed in SARS-CoV-2 infection and aging from Figure 2 that are either up-regulated in both SARS-Cov-2 infection and aging or down-regulated in both SARS-Cov-2 infection and aging. The prize of a terminal node equals the absolute value of its \log_2 -fold change in SARS-Cov-2-infected A549-ACE2 cells versus normal A549-ACE2 cells based on the data from [23]. Terminals and PPI data are processed using OmicsIntegrator2 [30] to output the disease *interactome*, i.e., the subnetwork induced by a Steiner tree, with drug targets indicated by green diamonds and terminal nodes colored according to their prizes. (b) Interactome obtained using this procedure. Genes are grouped by general function and marked with a cross if known to interact with SARS-Cov-2 proteins based on data from [6]. (c) 2-Nearest-Neighborhoods of nodes of interest (denoted by a red hexagon) in the interactome. A threshold was applied on the edge confidence to improve readability. Proteins known to interact with SARS-Cov-2 are denoted by blue squares, drug targets are denoted as green diamonds, terminal nodes are colored according to their \log_2 -fold change in SARS-Cov-2-infected A549-ACE2 cells versus normal A549-ACE2 cells, Steiner nodes appear in grey. (d) Table of drug targets and corresponding drugs in the interactome. Selected drugs are FDA approved, high affinity (at least one of the activity constants K_i , K_d , IC_{50} or EC_{50} is below $10\mu M$), and match the SARS-Cov-2 signature well (correlation > 0.86). The affinity column displays $-\log_{10}(\text{activity})$. Protein name corresponding to each gene is included.

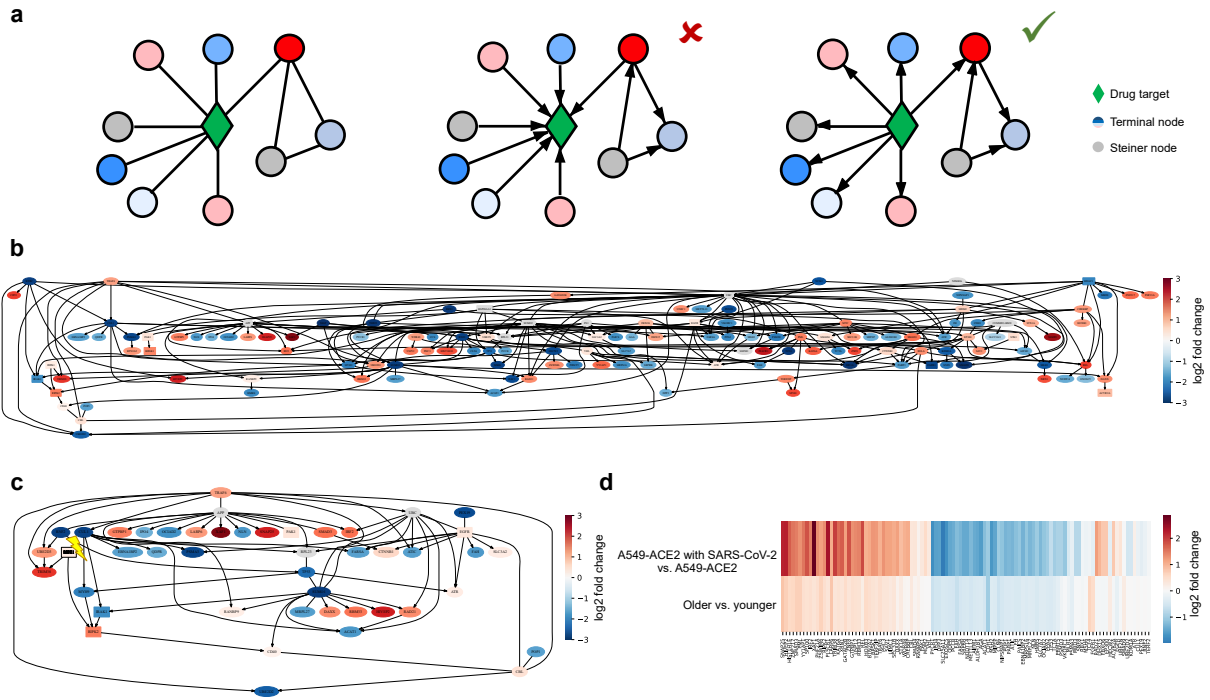


Figure 5: Causal mechanism discovery of potential drug targets. (a) In an undirected PPI network (left), edge directions for a particular drug target (green diamond) are unknown. Establishing causal directions is important since it is of interest to avoid drug targets that do not have many downstream nodes in the disease interactome (middle) and instead choose drug targets that have a causal effect on many downstream nodes in the disease interactome (right). (b) Causal network underlying the combined SARS-CoV-2 and aging interactome in A549 cells with gene targets of selected drugs in boxes (largest connected component shown). (c) Causal subnetwork of A549 cells corresponding to nodes within 5 nearest neighbors of RIPK1. The node color corresponds to the \log_2 -fold change of A549-ACE2 with versus without SARS-CoV-2. (d) Heatmap of \log_2 -fold change of genes that are downstream of RIPK1.

Supplementary Materials:
Causal Network Models of SARS-CoV-2 Expression and Aging
Identify Drugs for Repurposing

Anastasiya Belyaeva^{1#}, Louis Cammarata^{2#}, Adityanarayanan Radhakrishnan^{1#},
Chandler Squires¹, Karren Dai Yang¹, G.V. Shivashankar^{3,4}, Caroline Uhler^{1,3*}

¹Massachusetts Institute of Technology, U.S.A.

²Harvard University, U.S.A.

³ETH Zurich, Switzerland

⁴Paul Scherrer Institute, Switzerland

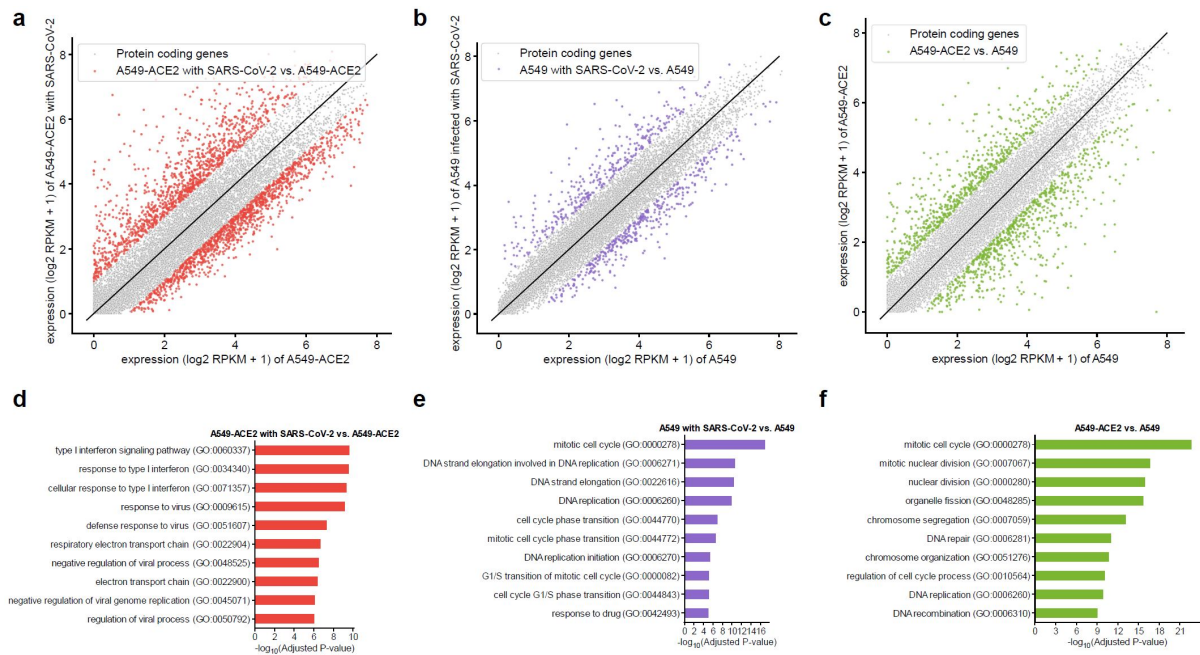
#Equal contribution.

*To whom correspondence should be addressed; E-mail: cuhler@mit.edu.

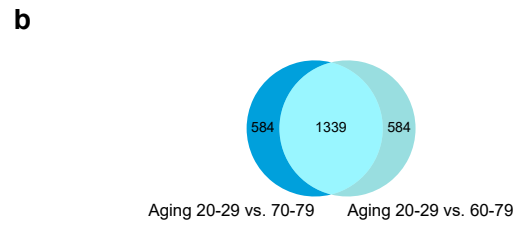
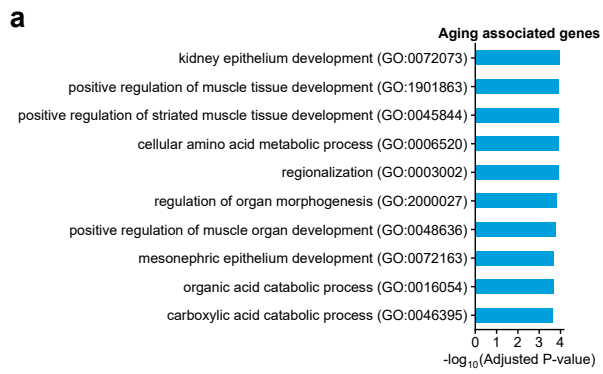
This PDF file includes:

Supplementary Figures S1 to S16
Supplementary Table S1
Supplementary Dataset 1 caption
References

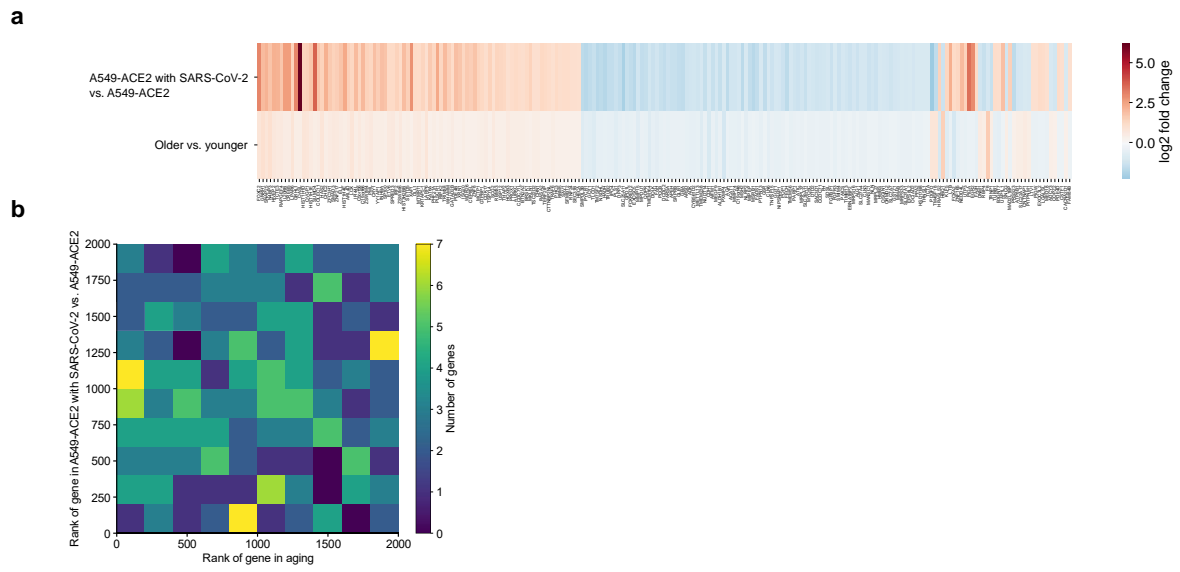
Supplementary Figures



Supplementary Fig. S1: (a) Gene expression of A549-ACE2 cells with and without SARS-CoV-2 infection, with differentially expressed genes in red. (b) Gene expression of A549 cells with and without SARS-CoV-2 infection, with differentially expressed genes in purple. (c) Gene expression of A549 cells with and without ACE2 receptor, with differentially expressed genes in green. (d) Top 10 gene ontology terms associated with differentially expressed genes between A549-ACE2 cells with and without SARS-CoV-2 infection. (e) Top 10 gene ontology terms associated with differentially expressed genes between A549 cells with and without SARS-CoV-2 infection. (f) Top 10 gene ontology terms associated with differentially expressed genes between A549 cells with and without ACE2 receptor. All gene ontology terms have adjusted p -value < 0.05 .



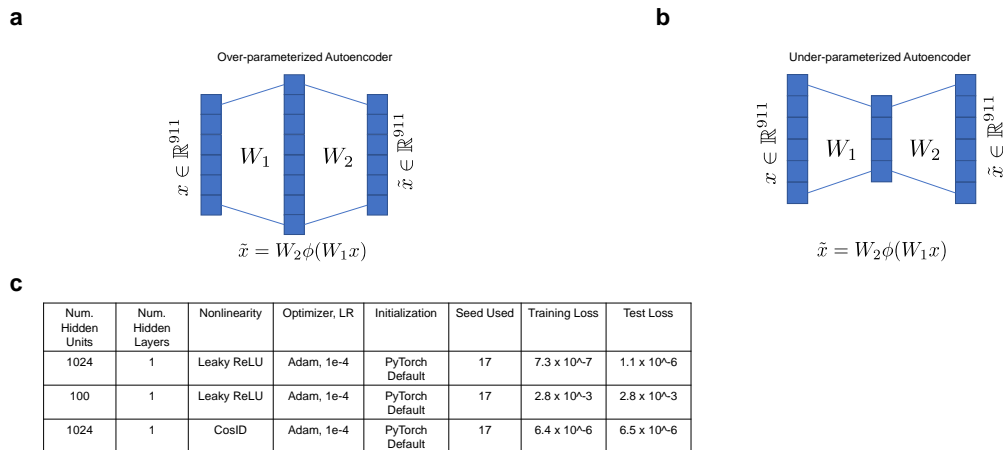
Supplementary Fig. S2: (a) Top 10 gene ontology terms associated with aging. (b) Venn diagram showing significant overlap between aging associated genes considering different definitions of older, specifically just individuals in the oldest category (70-79) or individuals that are 60-79.



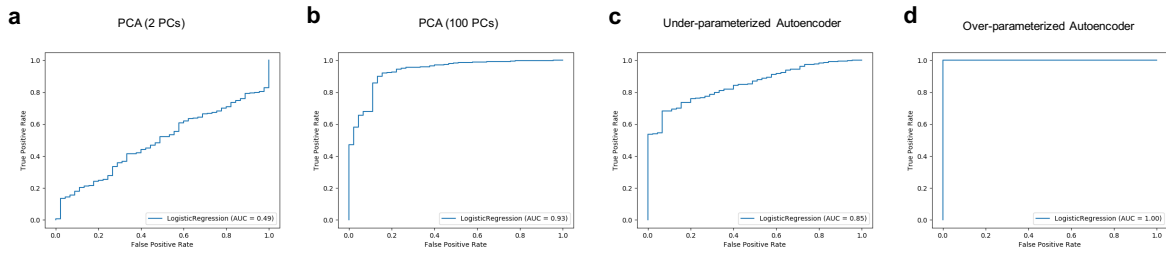
Supplementary Fig. S3: (a) Heatmap of \log_2 -fold changes of differentially expressed genes shared by SARS-CoV-2 and aging with gene names. (b) 2D histogram of the number of genes having a certain rank in aging and SARS-CoV-2 datasets.



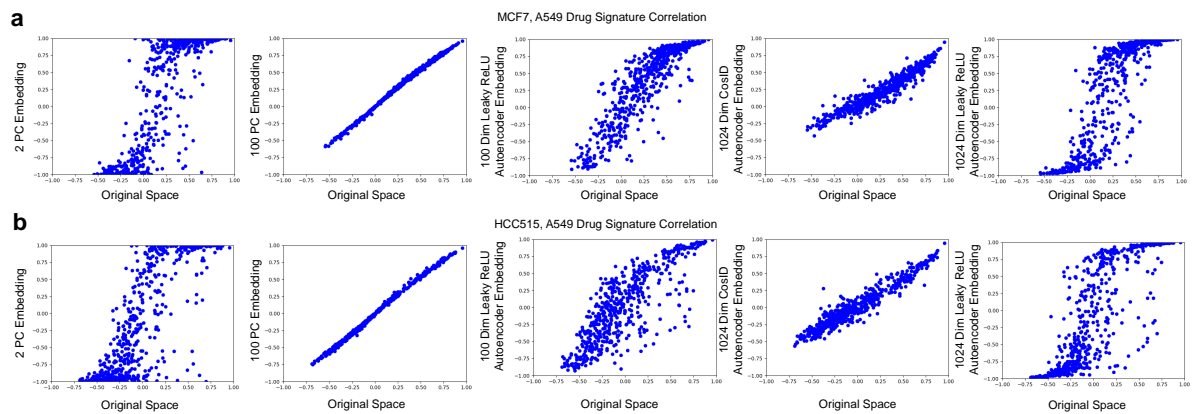
Supplementary Fig. S4: (a) UMAP of control and perturbations across all cell types in CMap. The effect of a perturbation on a given cell type is small relative to the differences between cell types. (b) Principal component analysis highlighting batch effects for the control samples of the A549 cell line from CMap. K-means clustering by gene expression vector is used to identify and remove batch effects (represented as red and blue clusters).



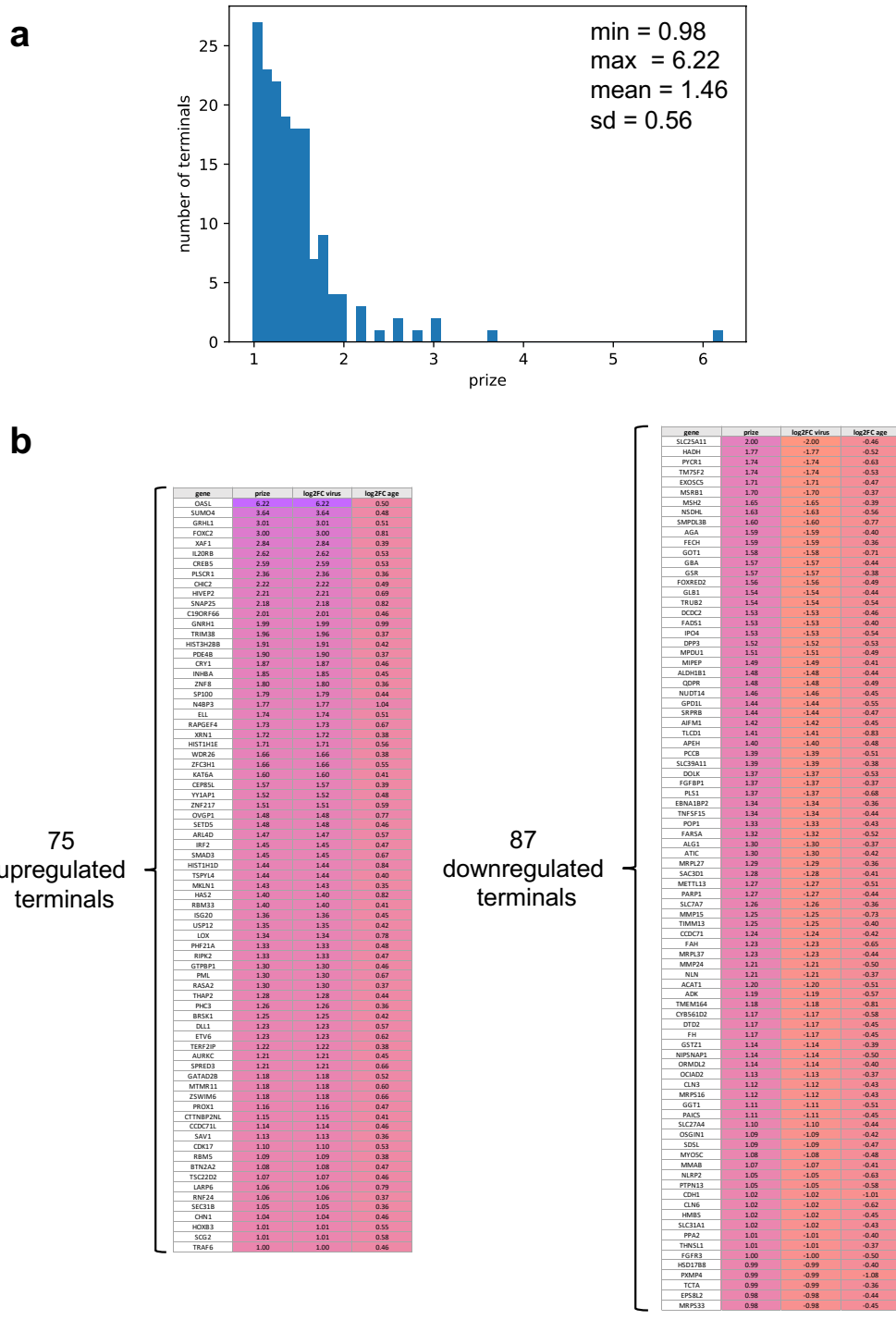
Supplementary Fig. S5: Overview of autoencoder architectures, optimization methods and hyperparameter settings considered. (a) Diagram representing an overparameterized autoencoder. While this autoencoder is capable of learning the identity function, training leads to a solution that better aligns drug signatures across cell types in the latent space. (b) Diagram representing an underparameterized autoencoder. While this architecture is most commonly used in practice, it does not align drug signatures as well in the latent space as its overparameterized counterpart; see Supplementary Fig. S7. (c) Details on the width, depth, nonlinearity, optimization method, learning rate, random seed, training loss and test loss for all architectures considered in this work.



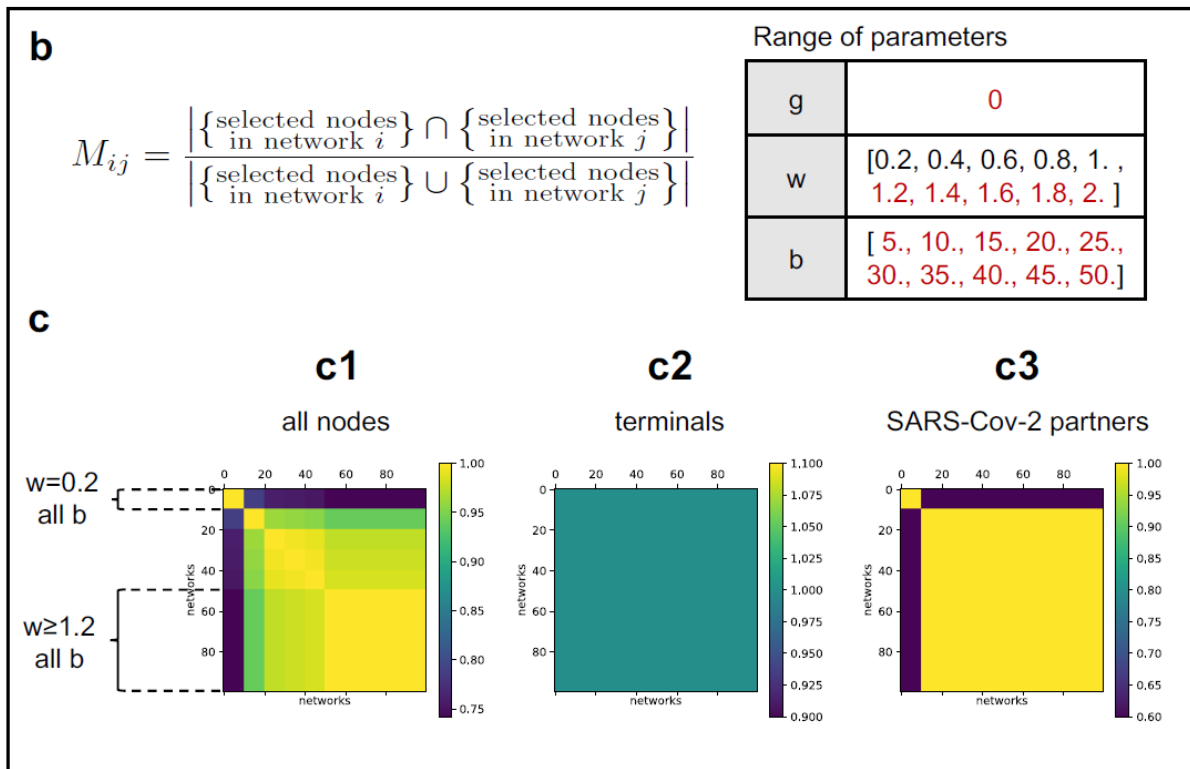
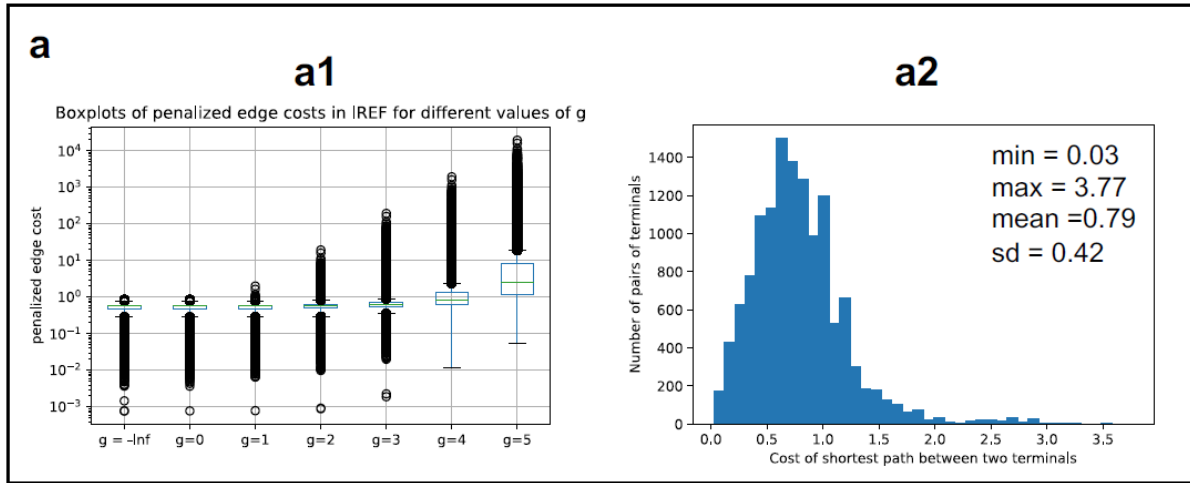
Supplementary Fig. S6: Receiver operating characteristic (ROC) curves for the agreement in classification between gene expression vectors and reconstructed gene expression vectors obtained using an embedding given by the first 2 principle components in (a), the first 100 principle components in (b), an underparameterized autoencoder in (c), and an overparameterized autoencoder in (d). While a logistic regression model trained to classify between 831 A549 control samples and 32893 A549 perturbation samples shows differences in predictions on original gene expression vectors versus underparameterized autoencoder reconstructions and reconstructions from the top 2 or 100 principal component, the overparameterized embedding allows near perfect reconstruction of the original gene expression vectors with no difference in predictions between using overparameterized embeddings for gene expression vectors and original gene expression vectors.



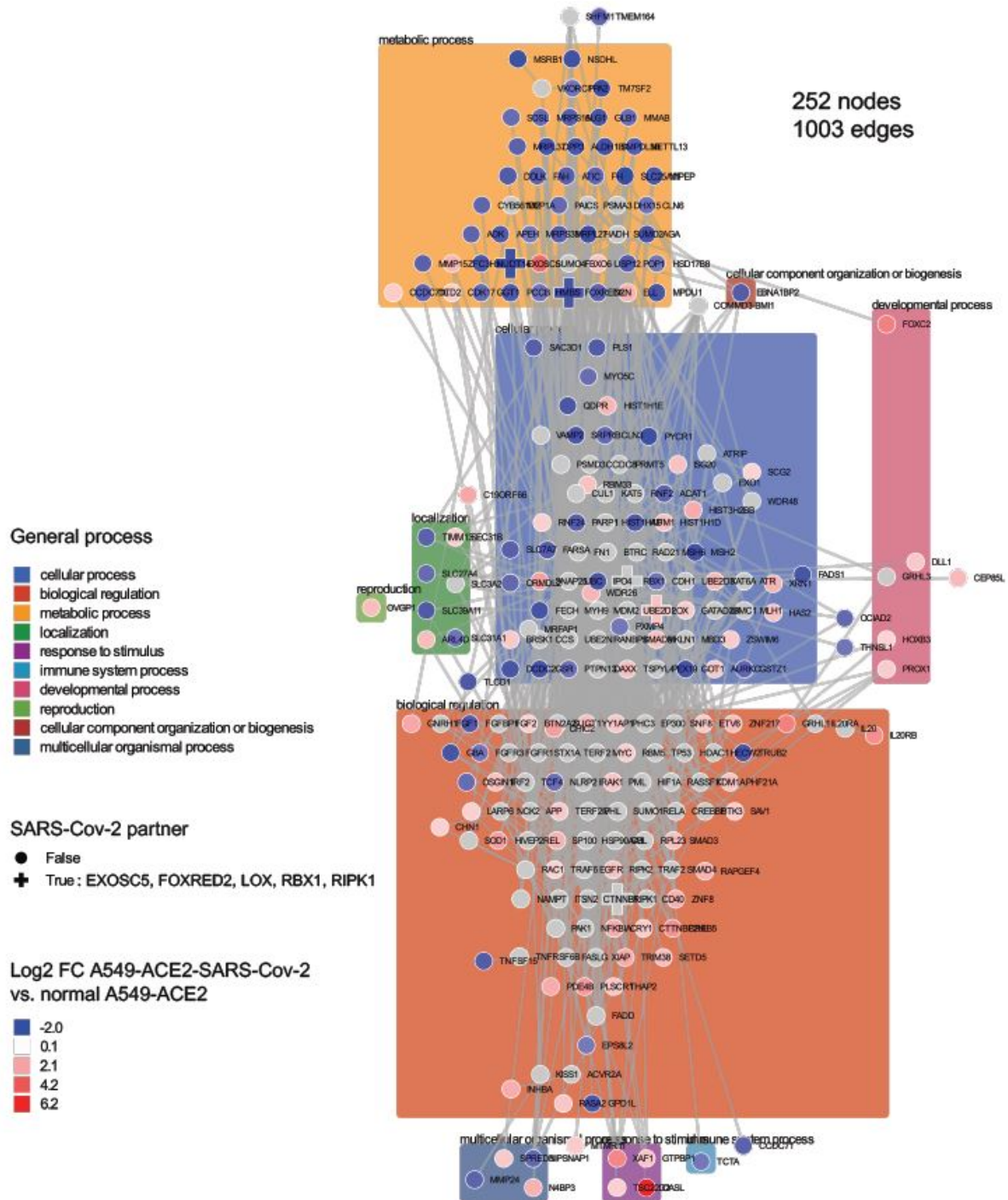
Supplementary Fig. S7: Comparison of drug signature alignment between A549 and MCF7 (top) and A549 and HCC515 (bottom) cell types upon using an embedding versus the original space. Embeddings provided include (from left to right) top 2 PCs, top 100 PCs, underparameterized leaky ReLU autoencoder, overparameterized cosid autoencoder, overparameterized leaky ReLU autoencoder. Embeddings from the overparameterized autoencoder with leaky ReLU activation better align drug signatures between these two pairs of cell types than any other embedding considered while still providing near perfect reconstruction of the original data.



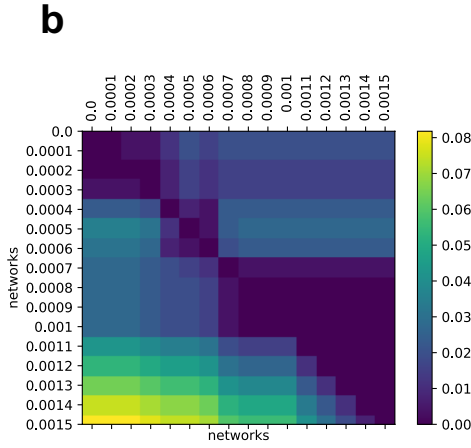
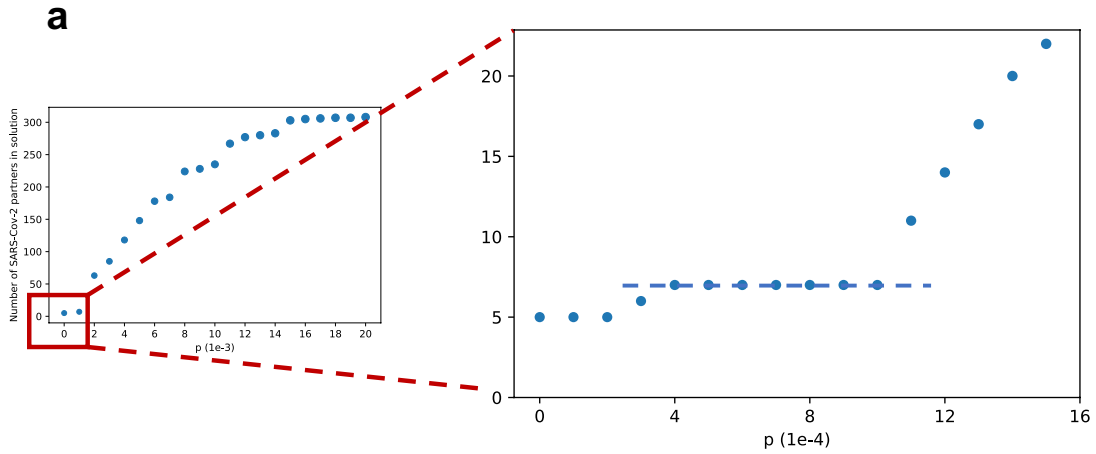
Supplementary Fig. S8: Terminal node selection for prize-collecting Steiner forest analysis. Terminal genes include 162 genes present in the IREF interactome that are either upregulated in both SARS-Cov-2 infection and aging or downregulated in both SARS-Cov-2 infection and aging. Each terminal gene is prized with its absolute log₂-fold change between SARS-Cov-2 infected A549-ACE2 cells and normal A549-ACE2 cells. (a) Histogram of prizes for terminal genes along with descriptive statistics. (b) Table of 75 terminal genes upregulated in both SARS-Cov-2 infection and aging (left) and table of 87 terminal genes downregulated in both SARS-Cov-2 infection and aging, along with prize and log₂ fold change information.



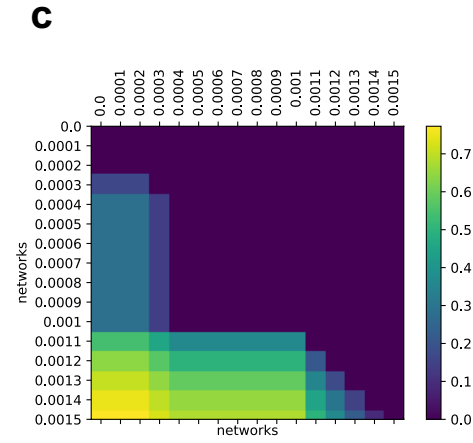
Supplementary Fig. S9: Parameter selection via sensitivity analysis for prize-collecting Steiner forest analysis. (a1) Boxplot of penalized edge costs in the IREF interactome for different values of g . The distribution of penalized edge costs are very similar for $g = -\infty$ and $g = 0$. For these values of g , the maximum penalized edge cost is upper bounded by 1. (a2) Histogram of shortest path cost between any two terminals in the IREF interactome for $g = 0$, along with descriptive statistics. (b) Range of parameters g , w and b used in sensitivity analysis. Red values indicate a stable range for the interactome obtained with the prize-collecting Steiner forest algorithm. We retain $g = 0$, $w = 1.4$ and $b = 40$ for our subsequent analysis. (c1-3) Heatmaps of the matrix M indexed for different types of selected nodes: all nodes (c1), terminal nodes (c2) and SARS-Cov-2 interaction partners (c3). Each row/column corresponds to a prize-collecting Steiner forest obtained from a given set of parameters ($g = 0, w, b$). A stability region for the prize-collection Steiner forest solution appears for $g = 0$, $w \geq 1.2$ and $b \in [5, 50]$.



Supplementary Fig. S10: Interactome obtained from the prize-collecting Steiner forest algorithm (with parameters $g = 0$, $w = 1.4$, $b = 40$) using the terminal gene list from Supplementary Fig. S8. The interactome contains 1,003 edges between 252 genes, five of which are known SARS-Cov-2 interaction partners (EXOSC5, FOXRED2, LOX, RBX1, RIPK1). Genes in the interactome are grouped by general process.

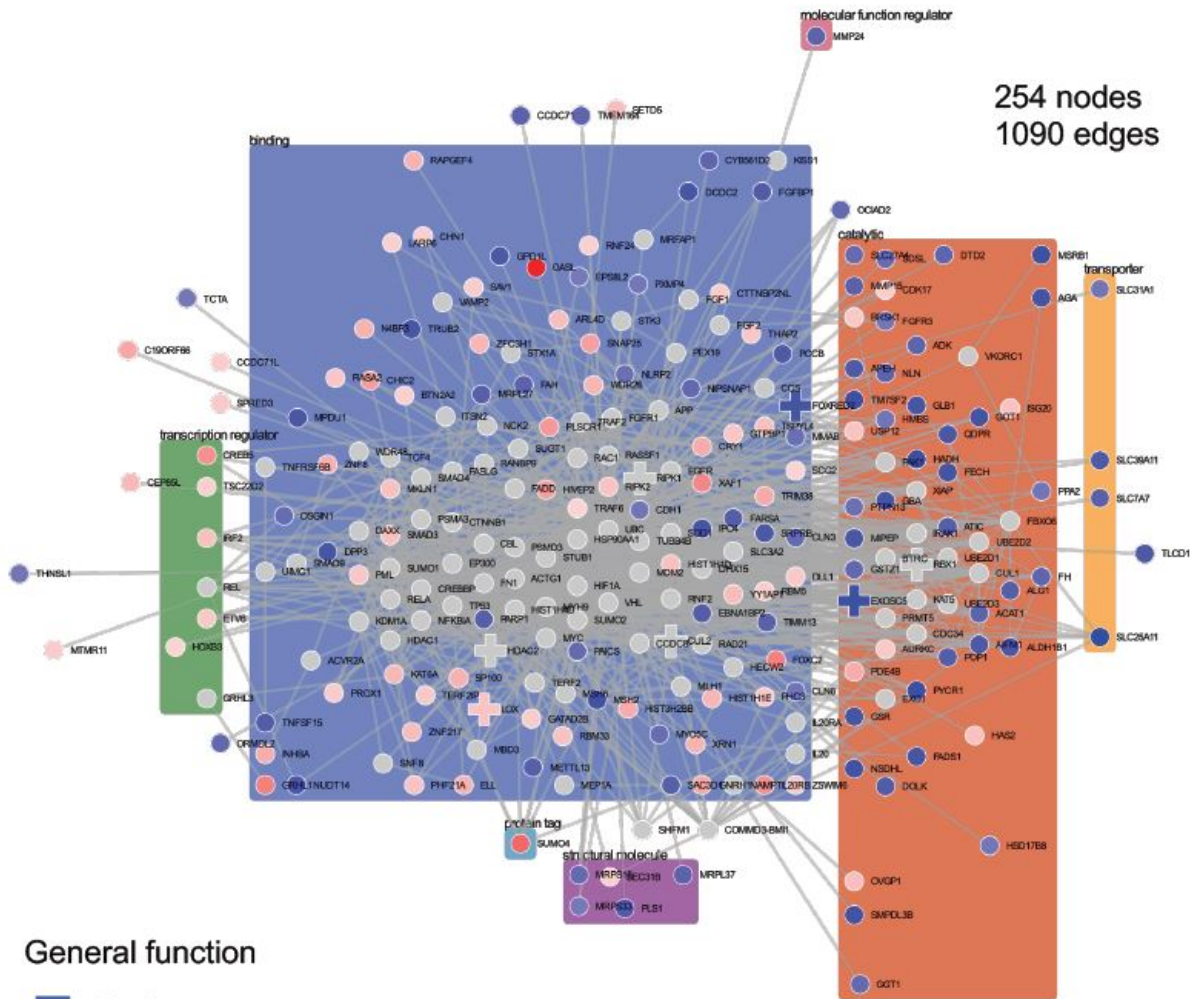


$$M_{ij} = \frac{|\{\text{all nodes in network } i\} \setminus \{\text{all nodes in network } j\}|}{|\{\text{all nodes in network } i\}|}$$



$$M_{ij} = \frac{|\{\text{SARS-Cov-2 partners in network } i\} \setminus \{\text{SARS-Cov-2 partners in network } j\}|}{|\{\text{SARS-Cov-2 partners in network } i\}|}$$

Supplementary Fig. S11: Selection of the prize p for non-terminal SARS-Cov-2 interaction partners (all but EXOSC5, FOXRED2 and LOX) via sensitivity analysis. (a) Number of SARS-Cov-2 interaction partners collected in the interactome obtained from the prize-collecting Steiner forest algorithm for different values of p ranging from 0 to 0.02. For $p > 0.02$, all known SARS-Cov-2 interaction partners present in the IREF network are collected in the final interactome. A stability region appears for $p \in [4 \cdot 10^{-4}, 10^{-3}]$ with 7 SARS-Cov-2 interaction partners collected. (b-c) Heatmaps of the matrix M indexed for different types of selected nodes: all nodes (b), and SARS-Cov-2 interaction partners (c). Each row/column corresponds to a prize-collecting Steiner forest obtained from a given set of parameters ($g = 0, w = 1.4, b = 40, p$). A stability region for the prize-collection Steiner forest solution appears for $g = 0, w = 1.4$ and $b = 40$ and $p \in [7 \cdot 10^{-4}, 10^{-3}]$. We retain $g = 0, w = 1.4, b = 40$ and $p = 8 \cdot 10^{-4}$ for our subsequent analysis.



General function

- binding
- catalytic
- transporter
- transcription regulator
- structural molecule
- protein tag
- molecular function regulator

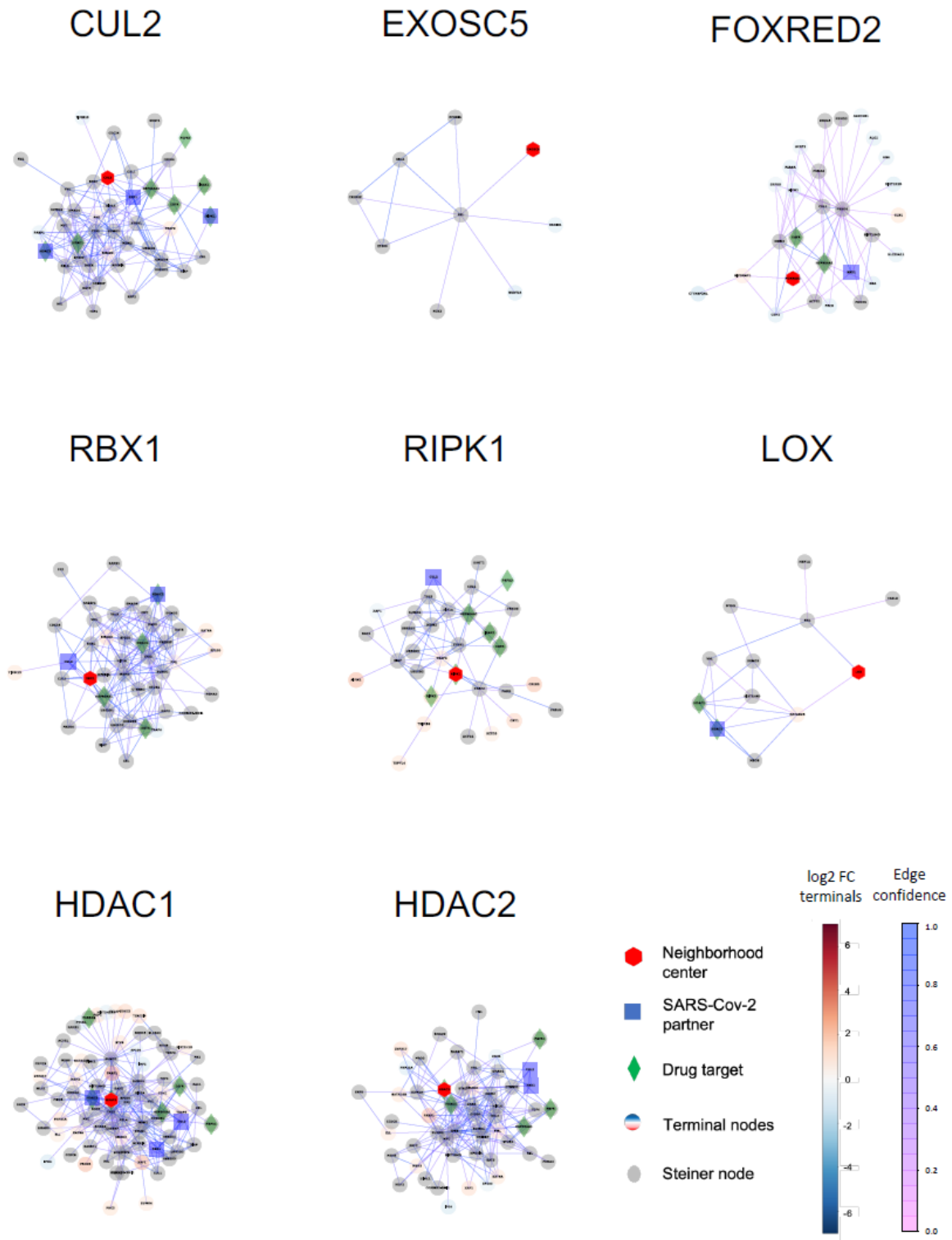
Log₂ FC A549-ACE2-SARS-Cov-2 vs. normal A549-ACE2

- -2.0
- 0.1
- 2.1
- 4.2
- 6.2

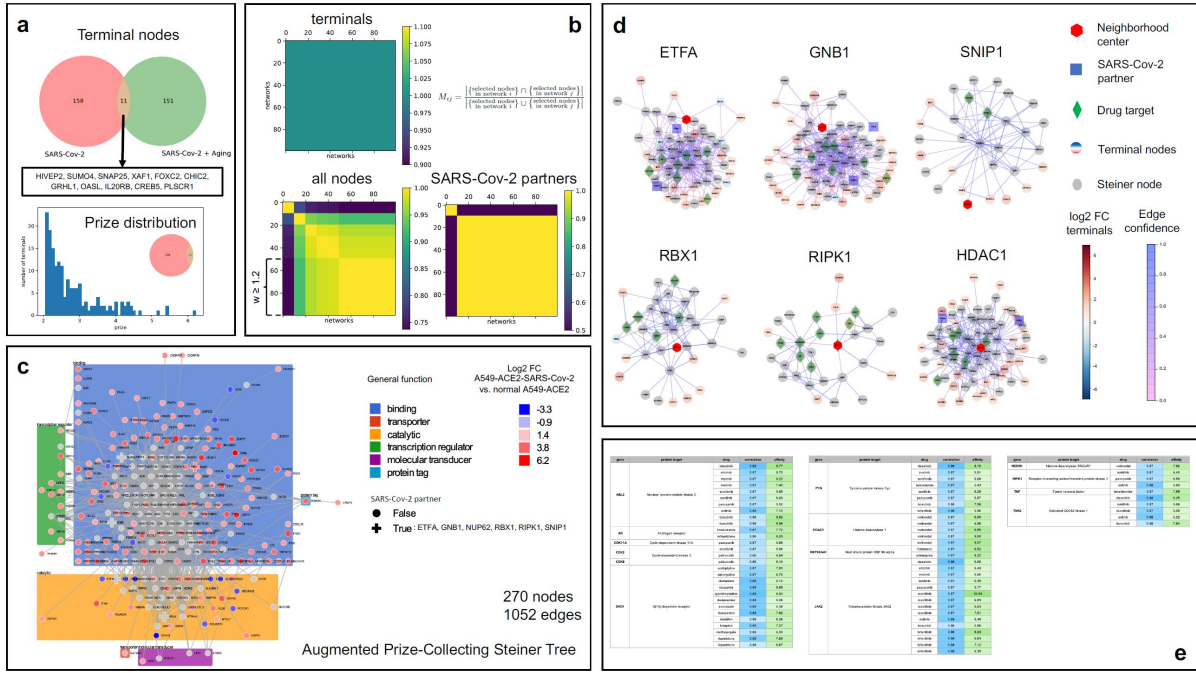
SARS-Cov-2 partner

- False
- ⊕ True : EXOSC5, FOXRED2, LOX, RBX1, RIPK1, CUL2, HDAC2

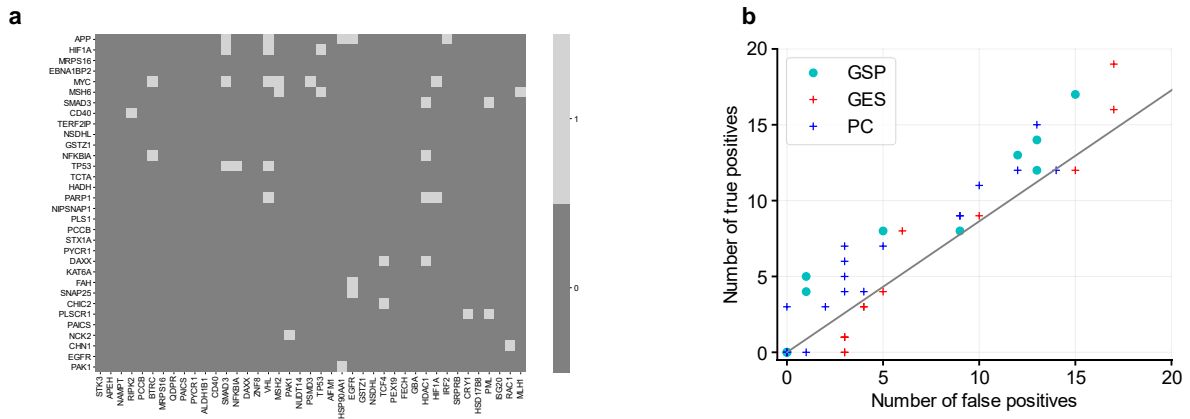
Supplementary Fig. S12: Interactome obtained from the prize-collecting Steiner forest algorithm (with parameters $g = 0$, $w = 1.4$, $b = 40$) using the terminal gene list from Supplementary Fig. S8 augmented with all other SARS-Cov-2 interaction partners prized with $p = 8 \cdot 10^{-4}$. The interactome contains 1,090 edges between 254 genes, seven of which being known SARS-Cov-2 interaction partners (EXOSC5, FOXRED2, LOX, RBX1, RIPK1, CUL2, HDAC2). Genes in the interactome are grouped by general function.



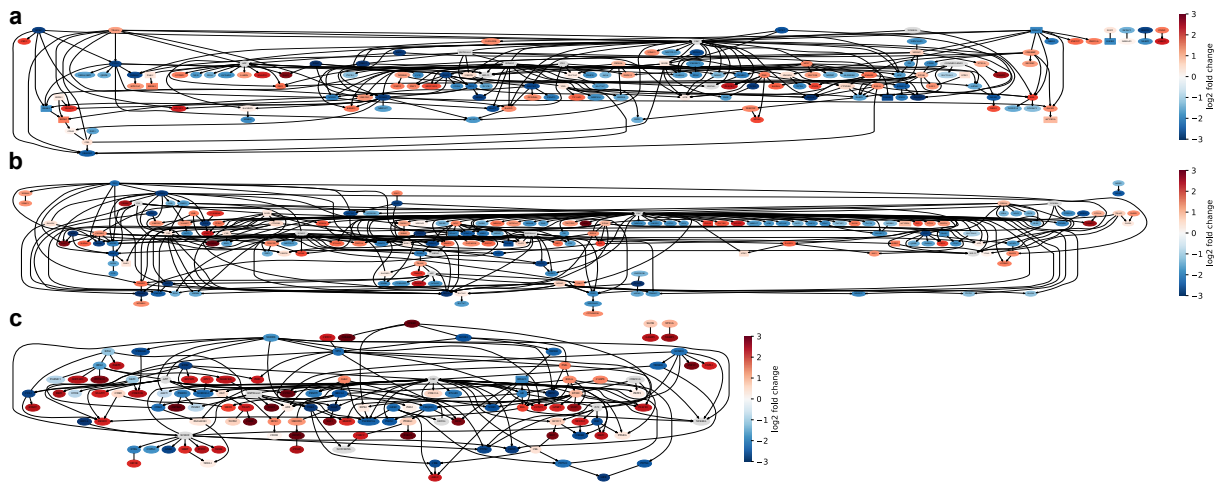
Supplementary Fig. S13: 2-Nearest-Neighborhoods of nodes of interest (denoted by a red hexagon) in the interactome of Supplementary Fig. S12 (parameters $g = 0$, $w = 1.4$, $b = 40$, $p = 8 \cdot 10^{-4}$). A threshold was applied on the edge confidence to improve legibility. Proteins known to interact with SARS-Cov-2 are denoted as blue squares, drug targets are denoted as green diamonds, terminal nodes are colored according to \log_2 -fold change in SARS-Cov-2-infected A549-ACE2 cells versus normal A549-ACE2 cells, Steiner nodes appear in grey.



Supplementary Fig. S14: Drug target discovery via prize-collecting Steiner forest analysis to identify putative molecular pathways linking differentially expressed genes in SARS-Cov-2 infection without taking into account age-related differential expression. (a) The general procedure to obtain the interactome is identical to the one described in Fig. 4a, with a different terminal gene list. (a) Terminal nodes and histogram of prize distribution. We consider 169 terminal nodes corresponding to genes differentially expressed in SARS-CoV-2 infection after removing the effect of the ACE2 receptor. Only 11 of these 169 genes belong to the terminal list used in Fig. 4. The prize of a terminal node equals the absolute value of its \log_2 -fold change in SARS-Cov-2-infected A549-ACE2 cells versus normal A549-ACE2 cells based on data from [23]. (b) Sensitivity analysis to choose the parameters w and b for the prize-collecting Steiner forest algorithm. We select $g = 0$, $w = 1.4$ and $b = 40$ corresponding to a robust solution for moderate changes in the parameters. (c) Interactome obtained using the prize-collecting Steiner forest algorithm. Genes are grouped by general function and marked with a cross if known to interact with SARS-Cov-2 proteins based on data from [6]. (d) 2-Nearest-Neighborhoods of nodes of interest (denoted by a red hexagon) in the interactome. A threshold was applied on the edge confidence to improve legibility. Proteins known to interact with SARS-Cov-2 are denoted as blue squares, drug targets are denoted as green diamonds, terminal nodes are colored according to \log_2 -fold change in SARS-Cov-2-infected A549-ACE2 cells versus normal A549-ACE2 cells, Steiner nodes appear in grey. (e) Table of drug targets in the interactome with the corresponding drugs. Selected drugs are FDA approved, high affinity (at least one of the activity constants K_i , K_d , IC_{50} or EC_{50} is below $10\mu M$), and match the SARS-Cov-2 signature well (correlation > 0.86). The affinity column displays $-\log_{10}(\text{activity})$. Protein name corresponding to each gene is included.



Supplementary Fig. S15: (a) Matrix Q of estimated effects of interventions (columns) on measured genes (rows) in A549 cells from CMap gene knockout and overexpression data with $Q_{ij} = 1$ representing that perturbing gene j effects gene i and hence that gene i is downstream of gene j . (b) ROC curve evaluating causal structure discovery methods GSP, PC and GES for predicting the effects of interventions in A549 cells. The performance of each algorithm is measured by sampling random causal graphs and measuring number of true positives and false positives. GSP performs significantly above random guessing with p -value of 0.0177, while PC achieves p -value of 0.0694 and GES a p -value of 0.5867. The grey line represents a random guessing baseline (not used for computation of p -value) based on the number of ground truth positives and negatives, calculated from Q and scaled to extend from (0,0) to span the entirety of the plot.



Supplementary Fig. S16: (a) Causal network corresponding to A549 cells. (b) Causal network corresponding to AT2 cells. (c) Causal network corresponding to A549 cells learned using PPI interactome obtained without considering age-associated genes as a prior. All non-singleton nodes are shown, gene targets of drugs selected via our computational drug repurposing pipeline are in boxes and the node color corresponds to the \log_2 -fold change of A549-ACE2 with versus without SARS-CoV-2.

Supplementary Tables

Drug name	% differentially expressed nodes downstream (A549)	% nodes downstream (A549 no age)	% nodes downstream (AT2)
afatinib	98.51	0.00	83.93
axitinib	98.51	0.85	83.93
bosutinib	98.51	0.00	83.93
dasatinib	98.51	0.00	83.33
erlotinib	98.51	0.00	83.33
imatinib	98.51	0.00	83.93
pazopanib	98.51	0.85	83.93
ruxolitinib	98.51	0.00	83.33
sorafenib	97.01	0.00	0.60
sunitinib	98.51	0.85	83.93
tofacitinib	1.49	0.00	0.00
belinostat	98.51	94.92	83.33
vorinostat	98.51	94.92	83.33
formoterol	98.51	94.92	83.33
primaquine	98.51	94.92	83.33
varденаfil	0.00	0.00	0.00
milrinone	0.00	0.00	0.00
docetaxel	98.51	0.00	83.33

Table S1: Percentage of nodes in the largest connected component of the corresponding causal graph that are targeted by each drug. For A549 cells, only genes that are associated with SARS-CoV-2 and aging are considered.

Supplementary Datasets

Dataset 1: Correlation of each drug applied to A549, MCF7 and HCC515 cells measured in CMap [2] with the direction from SARS-CoV-2 infection to normal in A549-ACE2 cells, calculated using autoencoder embedding, original space and top 100 principal components.